Hindawi
Journal of Electrical and Computer Engineering
Volume 2022, Article ID 2873053, 26 pages
https://doi.org/10.1155/2022/2873053

Research Article

STATCOM Controller Tuning to Enhance LVRT Capability of Grid-Connected Wind Power Generating Plants

Irene Ndunge Muisyo,[1] **Christopher Maina Muriithi**,[2] **and Stanley Irungu Kamau**[3]

[1]*Pan African University Institute for Basic Sciences,Technology and Innovation (PAUSTI), Juja, Kenya*
[2]*Murang'a University of Technology (MUT), Murang'a, Kenya*
[3]*Jomo Kenyatta University of Agriculture and Technology (JKUAT), Juja, Kenya*

Correspondence should be addressed to Irene Ndunge Muisyo; muisyoirene@jkuat.ac.ke

Received 17 March 2022; Revised 23 May 2022; Accepted 30 May 2022; Published 25 June 2022

Academic Editor: Gurvinder S. Virk

Copyright © 2022 Irene Ndunge Muisyo et al. This is an open access article distributed under the Creative Commons Attribution License, which permits unrestricted use, distribution, and reproduction in any medium, provided the original work is properly cited.

This paper investigates the utilization of a STATCOM to enhance the LVRT capability of wind power plants (WPPs) during grid faults. The STATCOM under investigation is tuned using the Water Cycle Algorithm (WCA), Particle Swarm Optimization (PSO), and a hybrid algorithm of both WCA and PSO. Simulations are conducted in MATLAB programming software, using the SimScape power system toolbox, where two test systems are investigated: a 9 MW WPP and the IEEE 39 bus test system. Performance analysis is done by investigating the ability of the WPPs to ride through grid voltage sags, with the incorporation of the STATCOM, independently tuned using WCA, PSO, and further with the hybrid WCA-PSO algorithm. To confirm the effectiveness of the proposed algorithm, simulation results for the three scenarios are compared. Results show that the LVRT capability of the German power system was met for L-G faults, for the 9 MW test system, whereas during LLL-G faults, the WPP only remained online for WCA and WCA-PSO tuned STATCOM. For the IEEE 39 bus system, the WPPs were able to ride through the LLL-G fault. In all scenarios, the WCA-PSO tuned STATCOM resulted in the least voltage, active, and reactive power overshoots.

1. Introduction

Over the last three decades, the utilization of renewable energy resources has been on the rise. This is attributed to the depletion of fossil fuel reserves, increase in energy demand, and environmental concerns. Wind energy is among the fastest-growing renewable energy resources [1]. The installed capacity of wind power generation globally was 743 GW by the end of 2020, which represented about 26% of renewable energy generation. China and US remain the world's largest onshore wind markets, together accounting for more than 60% of the new capacity in 2020 [2, 3]. Wind Energy Conversion Systems (WECSs) are either based on Fixed Speed Wind Turbines (FSWTs) or Variable Speed Wind Turbines (VSWTs). The FSWT configuration is simple but is unable to extract maximum power at varying wind speeds since its slip can only be varied over a small range. Most wind turbines today are based on the Variable Speed Wind Turbine (VSWT) technology, which utilizes power electronics to achieve improved efficiency and reduced mechanical stress for a wide range of wind speeds [4, 5].

The most common VSWT is the Doubly Fed Induction Generator (DFIG), due to its advantages such as variable speed capability, independent active and reactive power control, lower converter cost, and lower active power losses [4, 5]. However, the DFIG is sensitive to grid faults since its stator is directly connected to the power system. During grid faults, the transient stator flux sets up a surge current in the rotor circuit which can destroy the Power Electronic Converter (PEC). Voltage dips at the Point of Common Coupling (PCC) also reduce the converter capability to transfer power to the grid, which leads to increased DC link capacitor voltage [6, 7]. The PEC is usually protected by a crowbar, which short-circuits the rotor once triggered by a

fault. If the fault persists, the wind power generating plant is eventually disconnected from the grid [5, 6].

Previously, wind farms were allowed to disconnect from grids during power system faults. With increasing levels of wind power injection into grids, disconnecting wind power generation during faults can negatively affect the stability of a power system [1]. Therefore, power system operators worldwide have revised their Grid Code Requirements (GCRs) to incorporate the Low Voltage Ride Through (LVRT) capability of wind farms. LVRT capability is the ability of power plants to remain connected to the grid for a specific period during grid voltage sag conditions [8, 9]. Various techniques have been proposed in the literature to improve the LVRT capability of DFIG-based WPPs. These techniques include the following:

(i) The use of a crowbar which provides an additional path for the rotor current, thus the DFIG stays connected to the grid [10, 11]. The crowbar can also be integrated with an R–L circuit to confine both the rotor inrush current and DC link overvoltage within their predefined threshold [12, 13].

(ii) A DC chopper connected in parallel with the PEC to dissipate excess power in the DC bus, protecting semiconductor switches from an overvoltage [12, 14].

(iii) Series Dynamic Braking Resistors (SDBRs) activated during fault conditions to limit the rotor current, thus avoiding DC link capacitor overvoltage [10, 12].

(iv) Fault Current Limiters (FCLs) used to regulate the terminal voltage by injecting resistance into a circuit, limiting fault current [10, 12].

(v) Flexible AC Transmission System (FACTS) devices such as Dynamic Voltage Restorer (DVR) [15, 16], Static VAr Compensator (SVC) [8], and Static Synchronous Compensator (STATCOM) [17, 18].

Due to their reliability and fast response, FACTS devices are gaining popularity in their use to enhance the large-scale integration of renewable energy into grids. The DVR and STATCOM are the most utilized FACTS devices to enhance the performance of grid-connected WPPs. The DVR is seen to be robust; however, its rating should be the same as the rated output of the Wind Turbine Generator (WTG). Moreover, DVRs are expensive due to many ancillary components needed during installation [19, 20]. The STATCOM on the other hand can control output voltage independently of the AC system voltage, with a very fast response, and it is also easy to integrate into an existing power system [17, 18].

The STATCOM controller is based on a Proportional Integral (PI) controller which provides a simple design structure at an affordable cost. STATCOM controller tuning can be done using conventional methods such as Ziegler-Nichols (Z-N) and graphical tuning, or by intelligent optimization algorithms such as fuzzy logic (FL) based control, Genetic Algorithm (GA), and Particle Swarm Optimization (PSO) methods [21, 22]. With the advancement of artificial intelligence technologies, various optimization algorithms are increasingly being applied in controller parameter tuning and optimization. Intelligent optimization algorithms have merits of robustness and universality, but they also have challenges such as premature convergence or slow convergence rate [23].

This paper investigates the LVRT capability of DFIG-based, grid-connected WPPs with STATCOM utilization. The STATCOM controller is independently tuned using three algorithms, namely, the Water Cycle Algorithm (WCA), Particle Swarm Optimization (PSO), and a hybrid algorithm of both WCA and PSO. The main contribution of this research is the simultaneous tuning of all three STATCOM controllers, using the newly proposed Water Cycle Algorithm (WCA) and the hybridization of WCA and PSO algorithms which has not been applied previously in the dynamic tuning of STATCOM controllers. From the literature, LVRT capability enhancement of the IEEE 39 bus test system with wind power generation has not been conducted before.

The organization of the rest of this paper is as follows. Section 2 presents Wind Energy Conversion Systems (WECS) operation, whereas in Section 3, the STATCOM operation and tuning are explained. Section 4 presents the test system and simulation results, while conclusions and recommendations are given in Section 5.

2. Wind Energy Conversion Systems (WECS)

Wind Energy Conversion Systems (WECSs) convert the kinetic energy in wind into mechanical energy, using wind turbine rotor blades. The mechanical power developed by a wind turbine depends on the wind velocity and air density [1], expressed as

$$P_m = \frac{1}{2}\rho A_r v_w^3 C_p(\lambda, \beta), \tag{1}$$

where ρ is the air density (kg/m^3), A_r (πR^2) is the area swept by rotor blades (m^2), v_w is the wind speed (m/s), C_p is the power coefficient which is a function of Tip-Speed Ratio (TSR) λ, and the blade pitch angle (β) [6, 24]. The mechanical energy is then converted into electrical energy, which is fed to the grid. The Double Fed Induction Generator (DFIG) is investigated in this work, due to its advantages such as variable speed capability, independent active and reactive power control, lower converter cost, and lower active power losses [4, 5].

2.1. The Mathematical Modeling of DFIG. The DFIG has its stator directly connected to the grid, while its rotor is connected to the grid through a Power Electronic Converter (PEC), as shown in Figure 1 [8].

From Figure 1, the Rotor Side Converter (RSC) controls active and reactive power flow from the stator to the grid while the Grid Side Converter (GSC) maintains the DC link voltage constant, thus controlling the grid current [6, 8]. The

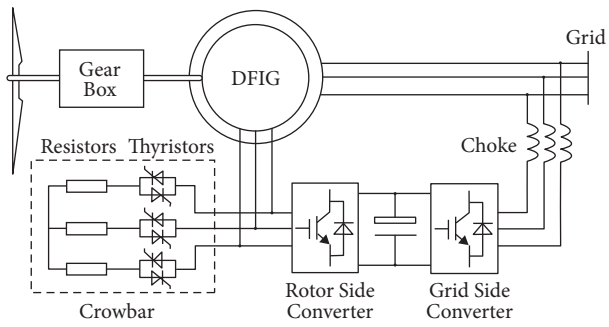

Figure 1: DFIG wind turbine [8].

equivalent circuit of a DFIG in the *d-q* reference frame is shown in Figure 2.

In Figure 2, subscripts d and q indicate direct and quadrature axis components, while s and r indicate stator and rotor quantities, respectively [19]. The d and q stator and rotor flux components are given by

$$\begin{aligned} \Psi_{sd} &= L_s i_{sd} + L_m i_{rd}, \\ \Psi_{sq} &= L_s i_{sq} + L_m i_{rq}, \\ \Psi_{rd} &= L_m i_{sd} + L_r i_{rd}, \\ \Psi_{rq} &= L_m i_{sq} + L_r i_{rq}, \end{aligned} \tag{2}$$

where L_s and L_r are the stator and rotor inductances, respectively, obtained using

$$\begin{aligned} L_s &= L_{s\sigma} + L_m, \\ L_r &= L_{r\sigma} + L_m. \end{aligned} \tag{3}$$

$L_{s\sigma}$ and $L_{r\sigma}$ are the stator leakage and rotor self-inductances, respectively, and L_m is the mutual inductance [19, 25]. The dq stator and rotor voltages are

$$\begin{aligned} v_{s\,d} &= R_s i_{s\,d} + \frac{d\Psi_{s\,d}}{dt} - \omega_e \Psi_{sq}, \\ v_{sq} &= R_s i_{sq} + \frac{d\Psi_{sq}}{dt} + \omega_e \Psi_{s\,d}, \\ v_{r\,d} &= R_r i_{r\,d} + \frac{d\Psi_{r\,d}}{dt} - (\omega_e - \omega_r)\Psi_{rq}, \\ v_{rq} &= R_r i_{rq} + \frac{d\Psi_{rq}}{dt} - (\omega_e - \omega_r)\Psi_{r\,d}, \end{aligned} \tag{4}$$

where v and i denote voltage and current, respectively, R is the resistance (Ω), Ψ is the flux linkage (V_s), ω_e is the supply angular frequency (rad/sec), and ω_r is the rotor angular frequency (rad/sec) [26, 27].

During normal operating conditions with constant stator voltage (V_s), the stator flux linkage (Ψ_s) stays almost constant; therefore, $d\Psi_s/dt$ can be neglected. However, during voltage sags, V_s dips and Ψ_s decreases proportionally with the grid voltage. The magnitude of the natural component of Ψ_s depends on the amplitude of voltage dip, and during faults, it generates a large EMF in the rotor windings. Thus, the more severe the voltage dip, the higher the induced EMF, which results in an overcurrent in the rotor windings. This can damage the PEC. In addition, low voltage at the PCC reduces the capacity of the GSC to transfer active power to the grid. This leads to excess power in the DC link capacitor, resulting in increased DC link voltage [25, 28].

Conventionally, the PEC is protected from rotor overcurrents using a crowbar, as shown in Figure 1. The crowbar in Figure 1 consists of a set of switches usually implemented between the rotor circuit and the RSC to provide a bypass for the high transient rotor current during faults [27]. Once triggered by DC capacitor overvoltage or rotor overcurrent, the crowbar short-circuits the RSC; thus, control of active and reactive power is lost. During this period, the DFIG absorbs reactive power from the grid, which negatively affects voltage at the PCC. If the fault persists, the DFIG is finally disconnected from the grid. Disconnecting large WPPs during grid faults contributes to active power imbalance, which may lead to cascading outages [25, 27].

2.2. Grid Codes for Wind Power Plants. Many countries have recently revised their grid codes to address the challenges of increased penetration of large wind power generation in modern power systems. Grid codes refer to technical specifications which describe the standards a power generation plant connected to a grid must meet, to ensure the safe and secure operation of the power system [10, 27]. Grid Code Requirements (GCRs) for wind power generating plants define the specifications wind power plants must satisfy when connecting to a power system. GCRs consist of static and dynamic specifications. Wind power static GCRs confer the steady-state behavior of wind power generating plants. On the other hand, the desired wind power generating plant's behavior during grid faults is stated in the dynamic requirements. These dynamic requirements include active power regulation and frequency operating range, voltage variation limits, Fault Ride Through (FRT) requirements, and grid support capability. A detailed description of the grid connection requirements for WPPs has been given in [27].

Power system operators have identified FRT capability during disturbances and reactive power control during steady-state conditions as the most important GCR in wind power integration into grids. FRT refers to the capability of wind power plants to remain connected to the grid during faults and provide reactive power support during such grid disturbances [14, 29]. FRT indicates the capability of large wind farms to stay connected to the grid for a brief period during faults. This ensures that for faults that can be cleared within a short duration, there is no loss of wind generation. FRT grid codes differ for each country based on the Transmission System Operator (TSO) requirements and grid strength. The minimum immunity of wind power plants to voltage fluctuations is denoted by voltage versus time characteristic curves, describing FRT requirements [19, 30].

FRT capability has two aspects i.e., High Voltage Ride Through (HVRT) during voltage swells, and Low Voltage Ride Through (LVRT) during voltage sags [19, 29]. Voltage sags are the most common in power system faults; hence,

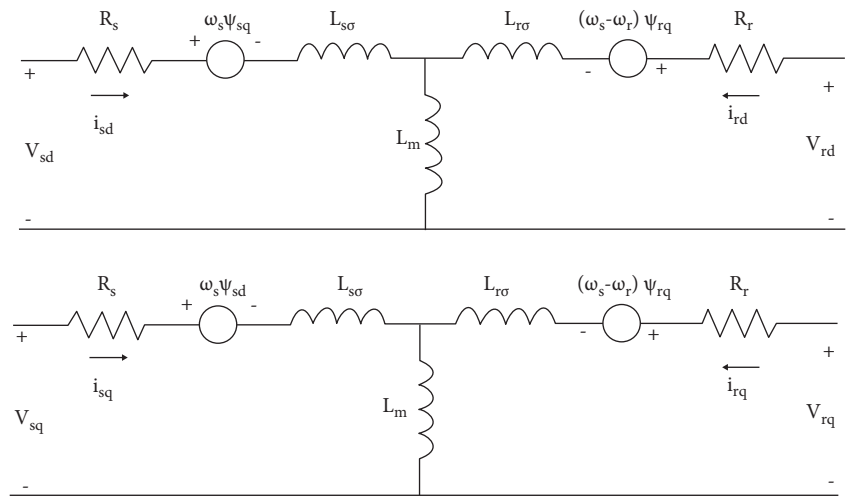

Figure 2: DFIG equivalent circuit [19].

LVRT capability is the most significant GCR for wind power generation. Voltage sags result from a sudden loss of large generating units, switching in large loads such as induction motors, energizing of transformers, and system faults [14, 29]. Recently, some countries have also included voltage-time profiles for conditions of swells in voltage in the grid codes. This requirement is referred to as the High Voltage Ride Through (HVRT) capability. Voltage swells result from single-phase short-term interruptions, reactive power overcompensation from capacitor banks, lightning strikes, or switching off large loads such as in response to voltage sag [30]. Since voltage sags are more frequent than swells, the LVRT capability of grid-connected wind power generating plants will be investigated in this work.

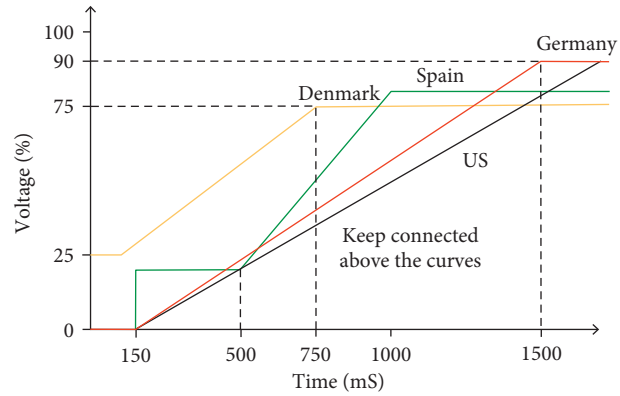

Figure 3: LVRT capability requirements for various countries [19].

2.3. Review of Grid Code Requirements for LVRT of Wind Farms. Low Voltage Ride Through (LVRT) capability is demonstrated by profiles of voltage and time duration for which a generator must stay connected or disconnected from the grid based on a reduction in the voltage levels during faults. LVRT characteristics for various countries are shown in Figure 3 [19].

From Figure 3, grid-connected WPPs must stay in operation if the voltage at the PCC remains above the solid line [15, 19]. From Figure 3, for instance, all wind farms connected to the German electric utility must withstand voltage dips up to 0% of nominal voltage at the PCC, for a duration of 150 ms. When the fault is cleared, the voltage at the PCC should recover to 0.9 p.u. within 1500 ms. To satisfy the Denmark grid code requirement, the WPP should remain connected for 100 ms when the terminal voltage drops to 20% of the nominal level, while the generator voltage should recover to 75% of the nominal level within about 700 ms. A summary of LVRT capability requirements for various countries is given in Table 1 [18, 31].

In the literature, several methods are being investigated for LVRT capability enhancement of DFIG-based WPPs. These methods can be broadly classified into protection circuit-based or reactive power injection-based LVRT schemes [13]. Protection circuits (crowbars, SDBRs, DC choppers, and FCLs) are applied to limit the rotor overcurrent and undesirable DC link overvoltage during grid disturbance. On the other hand, reactive power injecting devices inject or absorb reactive power, thus improving the transient performance of the DFIG-based WT. Reactive power injection schemes vary from simple techniques such as fixed capacitor/inductor to power electronic-based compensating devices [32].

With the ongoing advancement of power electronics, Flexible AC Transmission System (FACTS) devices are increasingly being adopted in modern power systems. FACTS devices consist of power electronic and static controllers which can be used to enhance controllability and increase power transfer capability in power systems. Depending on the desired compensation, FACTS devices can be connected in series such as the Dynamic Voltage Restorer (DVR) [10, 20], and the Static Synchronous Series Compensator (SSSC) [21], in shunt such as the Static Synchronous Compensator (STATCOM) [26, 33], or a combination of series and shunt such as Unified Power Flow Controller (UPFC) [21]. The Dynamic Voltage Restorer (DVR) and Static Synchronous Compensator (STATCOM) are the most utilized FACTS devices in enhancing the performance of

Table 1: LVRT capability requirements for various countries.

S. No.	Country	Voltage level	LVRT capability		
			Fault duration (ms)	Voltage drop level (%)	Recovery time (s)
1.	Denmark	DS/TS	100	25	1
2.	Ireland	DS/TS	625	15	3
3.	Germany	DS/TS	150	0	1.5
4.	Great Britain	DS/TS	140	15	1.2
5.	Spain	TS	500	20	1
6.	Italy	>35 kV	500	20	0.3
7.	United States	TS	625	15	2.3
8.	Ontario	TS	625	15	3
9.	Quebec	TS	150	0	0.18

DS: Distribution System, TS: Transmission System [31].

grid-connected WPPs [10, 13]. The DVR and STATCOM are Voltage Source Converter (VSC) based FACTS devices which can independently exchange active and reactive power with a grid. In this work, the STATCOM is investigated for enhancement of the LVRT capability of WPPs. The following section presents STATCOM operation and control.

3. STATCOM Operation and Control

The STATCOM is a shunt FACTS device used to inject or absorb reactive power to a specified bus. It comprises a Voltage Source Inverter (VSI), DC source, and a coupling transformer, connected in shunt with the AC system [33], as shown in Figure 4.

The VSI is the heart of a STATCOM consisting of self-commutating power electronic devices (GTO or IGBT), together with a reverse blocking diode in parallel. From Figure 4, V_g is the bus voltage, V_{st} is the VSI voltage, P is the active power of the VSI, and Q is the reactive power of the VSI [33, 34]. The DC input voltage from the capacitor is converted into a set of controllable three-phase AC output voltages by the VSI. Thus, the fundamental component of V_{st} is proportional to V_{dc}. VSI controller operation starts with a measurement system which obtains DC capacitor voltage V_{dc}, STATCOM reactive current I_{abc}, and bus line voltage $V_{g,abc}$ [28, 35], as shown in Figure 5.

From Figure 5, the Phase Locked Loop (PLL) system generates synchronizing signals (θ_{PLL}) for *abc/dq* transformation of $V_{g,abc}$ and I_{abc}. In the voltage regulator loop, the actual PCC bus voltage (V_g) is compared with the reference value (V_{ref}) and the difference is applied to the PI controller to generate the reference reactive current (I_{q_ref}). The current regulation loop compares injected or absorbed reactive current (I_q) with the reference value (I_{q_ref}) to produce the desired phase angle (α). α is the phase shift of STATCOM voltage (V_{st}) with respect to the grid voltage (V_g). The positive and negative voltages of the DC capacitor are maintained equal using offset ($\Delta\alpha$) from the DC voltage regulator [28, 35].

The STATCOM control circuit uses zigzag transformers to filter all odd harmonics up to the 45th. The star/delta transformer cancels out $5 + 12n(5, 17, 29, 41, ..)$ and $7 + 12n(7, 19, 31, 43, ..)$ harmonics. There is also a 15^0 phase

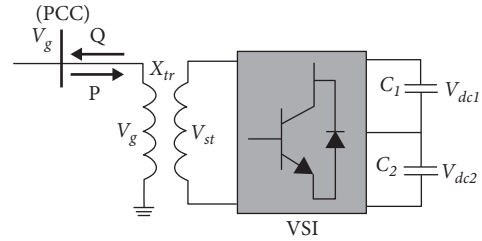

Figure 4: Equivalent circuit of the STATCOM [33].

shift between the two transformers, with the star side leading by 7.5^0 and the delta side lagging by 7.5^0, a shift that allows cancellation of $11 + 24n(11, 35, .)$, and $13 + 24n(13, 37, .)$ harmonics. All $3n$ harmonics are not transmitted by the transformers because of the delta and ungrounded star connection. The 23rd and 25th harmonics can also be minimized by adjusting the conduction angle (σ) to 172.5^0 ($180^0 - 7.5^0$). Thus, the first significant harmonics generated by the inverter will be 47th and 49th; an almost pure sine wave output is achieved [35, 36]. The switching pulses control the magnitude and phase of the VSI output voltage. The three regulators (voltage regulator, current regulator, and DC link voltage regulator) are based on a Proportional Integral (PI) controller [28, 35]. Their outputs are given by

$$I_{q_{ref}} = \left(V_{ref} - V_g\right)\left(K_P + \frac{K_I}{s}\right),$$

$$\alpha = \left(I_{qref} - I_q\right)\left(K_P + \frac{K_I}{s}\right), \tag{5}$$

$$\Delta\alpha = \left(V_{dc2} - V_{dc1}\right)\left(K_P + \frac{K_I}{s}\right).$$

The procedure of obtaining K_p and K_I which would result in the desired performance is called tuning. Controller tuning can be done using conventional methods such as Ziegler-Nichols (*Z-N*), pole placement, and graphical tuning or by intelligent optimization algorithms such as fuzzy logic (FL) based control, Genetic Algorithm (GA), and Particle Swarm Optimization (PSO), among other methods [18, 34]. Intelligent optimization algorithms are increasingly being applied in controller parameter tuning and optimization.

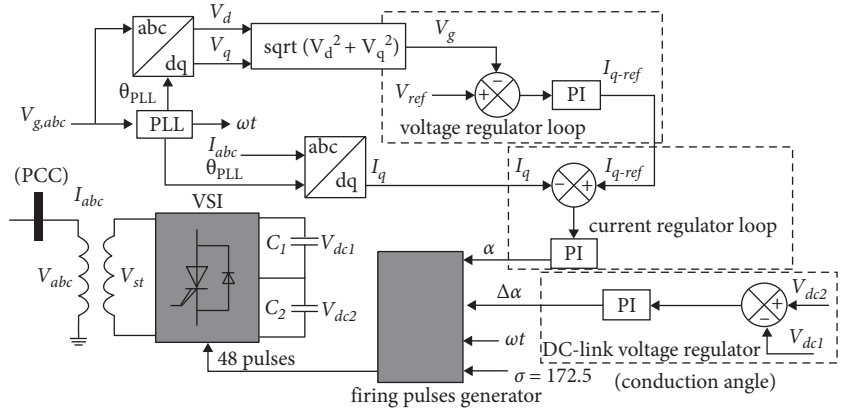

Figure 5: STATCOM control scheme [35].

These algorithms have merits of robustness and universality, but they also have challenges such as premature convergence or slow convergence rate [22, 23].

From the literature review, STATCOM controller tuning using intelligent optimization algorithms has not been investigated broadly. Rashad et al. in [17] use Artificial Neural Networks (ANNs) to tune a STATCOM, to improve the performance of a wind power plant during symmetrical faults. The performance of the wind farm with a STATCOM tuned by ANN was compared with that of a STATCOM tuned by the Multiobjective Genetic Algorithm (MOGA) and Whale Optimization Algorithm (WOA). From the results, ANN tuned STATCOM gave a better voltage profile for the wind farm during three-phase faults. The active power output of the wind farm with ANN tuned STATCOM was also greater than when the other two algorithms were used.

Kamel et al. in [18] investigate the ability of a STATCOM to enhance the FRT capability of DFIG wind turbines. STATCOM PI regulators were tuned using classical methods, fuzzy logic, PSO, Ant Colony Optimization (ACO), and the hybrid PSO-ACO. It was seen that the fuzzy control method and metaheuristic methods (PSO, ACO, PSO-ACO) resulted in a better dynamic performance for the STATCOM as compared to the classical tuning method. The authors observe that the hybrid PSO-ACO method was able to obtain proper gains for the STATCOM in a short time, and the method can be exploited to realize the dynamic behavior needed in FACTS devices.

Boulaoutaq et al. in [37] propose a scheme based on Active Disturbance Rejection Control (ADRC) strategy for a DFIG-based WT integrated with DVR. The DVR is connected in series with the DFIG output terminal and the utility grid to compensate for grid voltage disturbances, thus meeting LVRT requirements. The control scheme for DVR was designed using ADRC nonlinear control strategy. LVRT performance is investigated under a symmetrical voltage sag of 35% of the rated voltage which lasts for 150 ms. It is seen that the DVR controlled by the ADRC strategy effectively prevents the DFIG-based WT from experiencing transient voltages and currents and subsequently stays connected to the grid during the 35% voltage sag. Thus, a DVR controlled by the ADRC strategy can greatly enhance the LVRT capability of the DFIG-based WT under symmetrical voltage sag conditions. Despite its cost, DVR is highly recommended for already installed DFIG-WTs that do not have sufficient FRT capability.

Bakir and Kulaksiz in [34] model a Solar PV-Wind Hybrid Microgrid and incorporate a Genetic Algorithm (GA) tuned STATCOM to increase the system voltage stability. With the conventional controller, voltage fluctuation between ±10% is observed, as opposed to by ±8% witnessed when GA is used.

From the sample of ongoing research work, dynamic tuning of FACTS devices can be investigated for LVRT capability enhancement of WPPs. Little has been done on the dynamic tuning of STATCOM for LVRT enhancement of grid-connected WPPs. In this work, the Water Cycle Algorithm (WCA), Particle Swarm Optimization (PSO), and their hybrid technique WCA-PSO will be independently used to tune the three PI STATCOM regulators.

3.1. Problem Formulation. STATCOM controller tuning was converted to an optimization problem, with the aim of minimizing the error between the reference and measured values. Time domain integral error functions can be used as objective functions for metaheuristic optimization techniques. These include Integral of Squared Error (ISE), Integral of Absolute Error (IAE), and Integral of Time Absolute Error (ITAE) [18]. Control systems based on the ITAE function integrate the absolute error multiplied by time over a given period. Errors that exist for a long time are weighted more than those at the start of the response, which can reduce the settling time of the system.

When optimizing the ITAE function, settling time and overshoots are reduced faster than IAE and ISE tuning methods. The ITAE index is emerging as a powerful optimization objective function in heuristic optimization techniques. The only drawback is that the first response might be slow [38, 39].

The optimization problem was stated as follows:

Minimize

$$J(X) = \int_0^T \left|V_{ref} - V_g\right| t dt + \int_0^T \left|I_{qref} - I_q\right| t dt + \int_0^T \left|V_{dc2} - V_{dc1}\right| t dt, \quad (6)$$

subject to

$$K_{\min} \le K \le K_{\max}, \quad (7)$$

where $X = [K_{P1}, K_{I1}, K_{P2}, K_{I2}, K_{P3}, K_{I3}]$, T is the time range of the simulation, and t is the discrete solver step time ($50\mu s$). The constraints were obtained from a conventional STATCOM as given in Table 2.

The optimization algorithms minimize the total ITAE error value and return the final objective function value and the corresponding six gains at the optimal output. STATCOM controller gains were evaluated using the algorithms independently, and a performance comparison was done. The WCA, PSO, and WCA-PSO algorithms are described in the following sections.

3.2. Water Cycle Algorithm (WCA). The Water Cycle Algorithm (WCA) is a metaheuristic optimization algorithm inspired by the water cycle process. The algorithm is based on how rivers are created and how water travels to the sea. It was proposed by Hasanien and Matar in 2012 [40]. At the start of the WCA, an initial population of raindrops (N_p) is generated. The cost function of each raindrop is evaluated using (6), and the costs are sorted in ascending order. The best raindrops (N_{sr}) are assigned to a number of rivers (N_r) and one sea, i.e.,

$$N_{sr} = N_r + \underbrace{1}_{\text{sea}}. \quad (8)$$

In the optimization problem, the sea position is the optimal solution. The remaining population, N_{st}, includes streams that can flow to the rivers or directly to the sea, given by

$$N_{st} = N_p - N_{sr}. \quad (9)$$

Streams are allocated to rivers or the sea, based on the flow intensity of raindrops given by

$$NS_n = \text{round}\left\{\left|\frac{C_n}{\sum_{i=1}^{N_{sr}} C_i}\right| x N_{st}\right\}, n = 1, 2, \ldots, N_{sr}, \quad (10)$$

where NS_n is the number of streams flowing into certain rivers and seas [41, 42]. Streams move toward rivers and rivers toward the sea. Updated positions for the streams and rivers are given by

$$\begin{cases} X_{\text{stream}}^{i+1} = X_{\text{stream}}^{i} + r \text{ and } xCx\left(X_{\text{river}}^{i} - X_{\text{stream}}^{i}\right), \\ X_{\text{river}}^{i+1} = X_{\text{river}}^{i} + r \text{ and } xCx\left(X_{\text{sea}}^{i} - X_{\text{river}}^{i}\right), \end{cases} \quad (11)$$

where rand $\in [01]$ and C is greater than 1. Costs of the new positions are evaluated again, and if the stream cost is less than the river cost, their positions are exchanged. If the cost of a river is less than that of the sea, their positions are exchanged. To avoid premature convergence, evaporation is conducted. We check whether the river or stream is sufficiently close to the sea to enable evaporation. Raining and evaporation are conducted if

$$\left|X_{\text{sea}}^{i} - X_{\text{river}}^{i}\right| < d_{\max}, \quad (12)$$

where $i = 1, 2, \ldots, N_{sr-1}$ and $d_{\max}$ is a small number, updated as

$$d_{\max}^{i+1} = d_{\max}^{i} - \frac{d_{\max}^{i}}{\text{max\_iter}}, \quad (13)$$

where $i = 1, 2, \ldots,$ max_iter. The optimization algorithm will continue with the search process until termination criteria are met. Raindrops at the optimal solution correspond to the optimal PI parameters [42, 43]. A flowchart of the WCA is given in Figure 6.

The parameters used in WCA optimization in this work are given in Table 3.

The WCA has been observed to be efficient and simple compared to other methods. It has also shown superior performance in terms of convergence, computation, and precision [40, 43].

Table 2: STATCOM PI gain constraints [35].

PI controller	Constraints
AC PI voltage regulator	$5 \le K_{P1} \le 20, 1000 \le K_{I1} \le 2000$
AC PI current regulator	$0.3 \le K_{P2} \le 10, 10 \le K_{I2} \le 20$
DC PI voltage regulator	$0.0001 \le K_{P3} \le 1, 0.02 \le K_{I3} \le 1$

3.3. Particle Swarm Optimization (PSO). Particle Swarm Optimization (PSO) algorithm is a biologically inspired computational search and optimization method developed in 1995 by Eberhart and Kennedy. The algorithm simulates the behavior of birds or fish when looking for the place with the most adequate food. The PSO algorithm starts by randomly generating particles in the search space. Next, the fitness value of each particle is evaluated, and the position corresponding to the best fitness value is called the local best position. The local best of all particles is compared and the best position in the swarm is defined as the global best. At every iteration, the termination criteria are checked, and if not met, an update of the velocity and position of all particles is done [44]. The velocity of particles is given by

$$V_{k+1}^{i} = wV_k^i + C_1 r_1\left(P_k^i - X_k^i\right) + C_2 r_2\left(P_k^g - X_k^i\right), \quad (14)$$

while the position of individual particles is updated by

$$X_{k+1}^{i} = X_k^i + V_{k+1}^i, \quad (15)$$

where X_k^i is the particle position, V_k^i is the particle velocity, P_k^i is the individual particle best position, P_k^g is the swarm best position, w is the weight inertia used to ensure convergence, C_1 and C_2 are the cognitive and social parameters, and r_1 and r_2 are random numbers between 0 and 1 [45]. The flowchart of the PSO algorithm is shown in Figure 7.

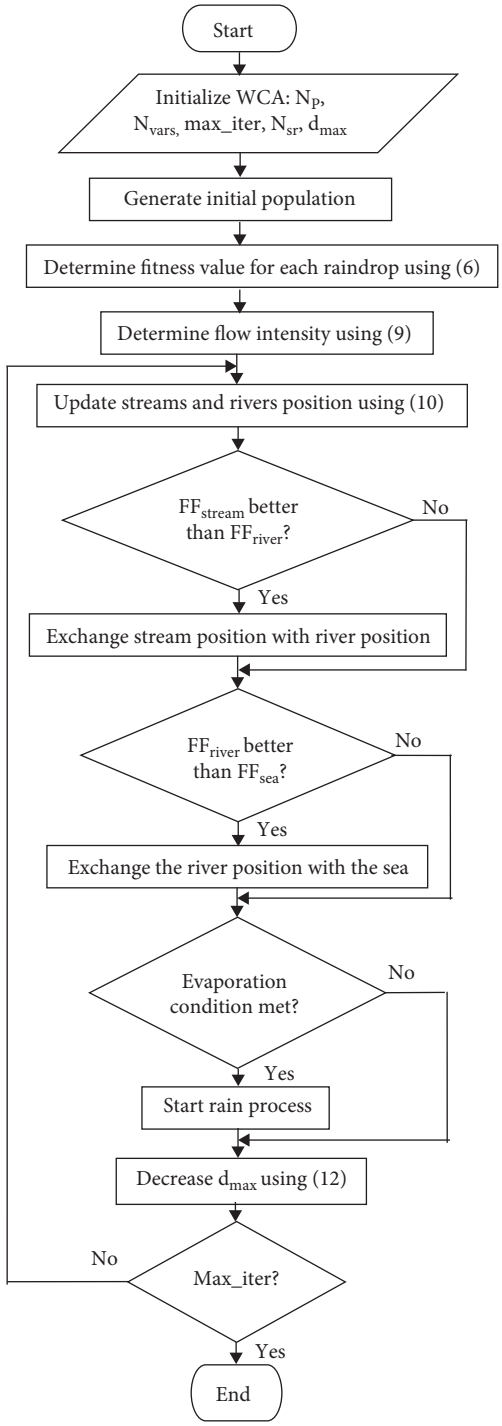

Figure 6: Water Cycle Algorithm flowchart [42].

Table 3: WCA parameters [43].

Parameter name	Variable	Value
No. of variables	N_{vars}	6
Population size	N_p	50
No. of rivers + sea	N_{sr}	4
Evaporation condition constant	d_{max}	10^{-16}
Maximum no. of iterations	Max_iter	100

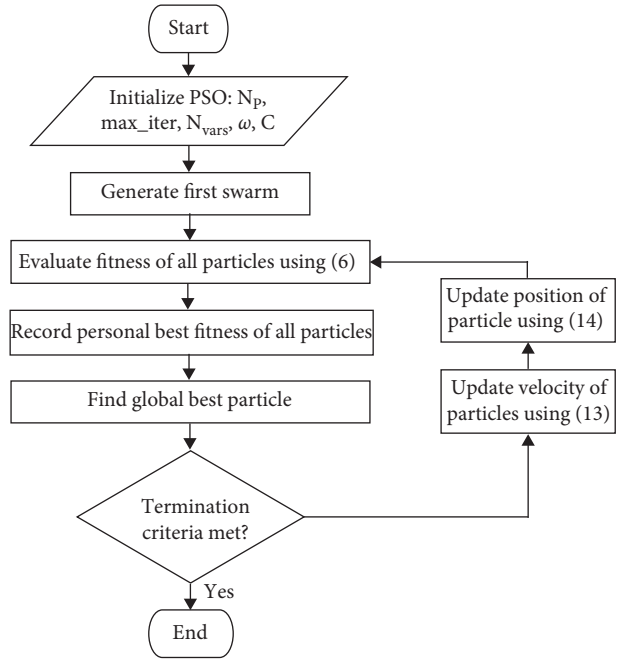

Figure 7: PSO flowchart [45].

Table 4: PSO parameters [45].

Parameter name	Variable	Value
Population size	N_P	100
Maximum number of iterations	Max_iter	100
No. Of variables	N_{vars}	6
Minimum inertia weight	w_{min}	0.4
Maximum inertia weight	w_{max}	0.9
Cognitive component	C_1	1.4
Social component	C_2	1.4
Random numbers	r_1, r_2	U (0,1)

The PSO parameters used in this work are given in Table 4.

The PSO algorithm has been gaining popularity due to its simple structure and efficiency. Additionally, it outperforms gradient-based optimization methods which require the optimization problem to be differentiable. However, the PSO algorithm can result in suboptimal solutions in the event a particle gets stuck in a local optimum [46, 47].

3.4. WCA-PSO Hybridization. The WCA was hybridized with PSO to take advantage of the strengths of each algorithm. In this hybrid, the WCA first explores the search place to identify the most promising region, thus ruling out the challenge encountered by the PSO of particles being stuck in a local optimum. Next, starting with the solution obtained by WCA, the PSO is introduced to continue with the search until termination criteria are met. The flowchart of the hybridized WCA-PSO algorithm is shown in Figure 8.

The parameters used in this work for the hybridized algorithm are given in Table 5.

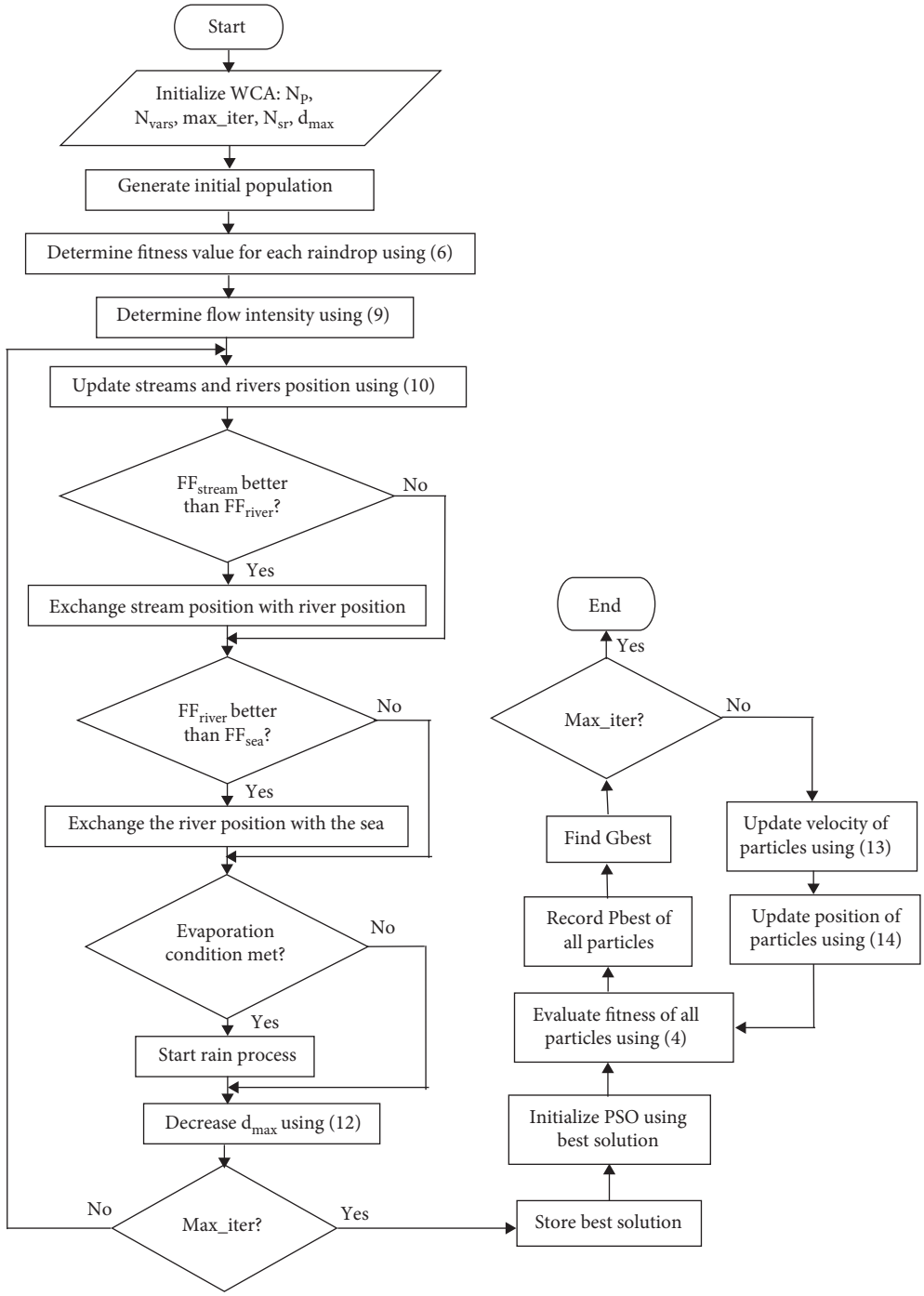

Figure 8: WCA-PSO flowchart [42, 45].

Each algorithm was independently used to tune the STATCOM. Different PI gains were obtained, and the test results are discussed in the following section.

4. Test System and Results

4.1. 9 MW Test System. LVRT capability investigation is done for a power system integrated with a 9 MW DFIG-based wind power generating plant. The test system was developed by aggregating six, 1.5 MW DFIG wind turbines into a 9 MW WPP. The output of the wind power generating plant is injected into a 25 kV distribution system through a three-phase 12 MVA transformer. The wind turbine and induction generator parameters are presented in Tables 6 and 7, as obtained from [18]. A single line diagram of the test system is shown in Figure 9.

A medium transmission line of 30 km length connects the WPP to a 120 kV grid through a three-phase 47 MVA transformer at the bus feeder B_2. The transmission line parameters are found in Table 8. During normal operating

Table 5: WCA-PSO parameters [42, 45].

Parameter name	Variable	Value
No. of variables	N_{vars}	6
Population size	N_{pop}	50
Maximum no. of iterations (PSO)	Max_iter	50
Maximum no. of iterations (WCA)	Max_iter	50
Minimum inertia weight	w_{min}	0.4
Maximum inertia weight	w_{max}	0.9
Cognitive and social components	$C_1 = C_2$	1.4
Random numbers	r_1, r_2	U (0, 1)
No. of rivers + sea	N_{sr}	4
Evaporation condition constant	d_{max}	10^{-16}

Table 6: Wind turbine parameters [18].

Wind turbine parameters	
Rated capacity	9 MW (6 turbines × 1.5 MW)
Cut-in wind speed	3.5 ms/
Cut-out wind speed	25 m/s
Rated wind speed	12 m/s
No. of blades	3
Rotor diameter	82.5
Area swept	5346 m^2
Rotor speed	10.1–18.7 rpm

Table 7: Wind generator parameters [18].

DFIG parameters	
P_{rated}	9 MW
V_{rated}	575 V
r_s	0.00706
r_r	0.005
l_{ls}	0.171
l_{lr}	0.156
L_m	2.9
pf	0.9

conditions, the reactive power output of the DFIGs is regulated at zero MVAr to maintain a unity power factor connection. The wind turbines have a protection system monitoring voltage, current, and machine speed.

The test system was independently subjected to L-G and LLL-G, 100% voltage sags on the grid side for 150 ms, to investigate the German utility LVRT capability requirement. The German LVRT GCR is investigated since it is very tough to satisfy, as it demands WPP LVRT capability at a voltage level of 0 p.u., at the PCC. LVRT GCRs for other utility grids given in Table 1 can also be investigated. A constant wind speed of 12 m/s is assumed since the fault duration is short, for noticeable wind speed variations. Simulation time was taken to be 20 seconds, and faults were introduced at $t = 15$ seconds and cleared at $t = 15.15$ seconds. The implementation was conducted in MATLAB 2018b programming software, using the SimScape power system toolbox. Simulations were done on a Lenovo ThinkPad P53s, powered by Intel Core i7-8th gen, 48 GB RAM, 512 GB SSD.

A STATCOM was installed at buses B_1 and B_2 independently, as voltage profile and reactive power injection were monitored, to determine the optimal location and size of the STATCOM. B_2 was obtained as the most optimal location, while the optimal size of the STATCOM was obtained as ±100 MVA. A conventional 25 kV, 100 MVA STATCOM was adopted, whose classical gains and parameters obtained from [35] were used, presented in Table 9. Utilizing random streams/particles within the search space as initial inputs, and constraints for the search space previously given in Table 2, WCA, PSO, and WCA-PSO algorithms were used to tune the STATCOM, based on the objective function previously given in (6). The PI gains obtained for the three tuning algorithms are presented in Table 10.

The PI gains given in Table 10 for PSO, WCA, and WCA-PSO tuning algorithms are compared with gains obtained in [18], where the authors used Ant Colony and Particle Swarm Optimization algorithms. As expected, a slight deviation in tuned parameter results is observed, since metaheuristic optimization algorithms do not guarantee reproducibility. Simulations were conducted on the test system with each STATCOM independently incorporated, and performance analysis was done. In the next section, the dynamic performance of the power system with the proposed STATCOM controller is discussed.

4.2. L-G Fault

4.2.1. WPP Active Power Output. The active power output of the WPP for *L-G* 100% grid voltage sag of 150 ms is given in Figure 10.

At $t = 15$ s, a fault is simulated in which grid voltage drops to 0p.u. for 150 ms. From Figure 10, without STATCOM, active power output drops from 8.8 MW to −1 MW, due to the low voltage at the connection bus. Once the DFIG protection system detects an undervoltage, the crowbar is activated. The RSC is bypassed and the DFIG acts as a Squirrel Cage Induction Generator (SCIG). As the voltage drops, the active power supply to the grid falls to zero and the WPP draws active power from the grid. When either conventional or tuned STATCOM is incorporated, voltage support is provided at the PCC, and the WPP maintains active power output during the fault period. LVRT capability requirements of German utility state that grid-connected wind power plants should be able to withstand voltage sags of up to 100% for 150 ms, a requirement met for all scenarios. Without a STATCOM, active power fluctuations are larger compared to tuned models.

4.2.2. Voltage Magnitude at WPP Terminals. The voltage profile at WPP terminals is shown in Figure 11, for *L-G* 100% voltage sag of 150 ms on the grid side.

From Figure 11, voltage fluctuations are seen at the WPP terminals. Voltage magnitude drops from 1 p.u. to 0.76 p.u. without STATCOM, whereas for the tuned models, the lowest voltage magnitude is 0.9 p.u. The voltage fluctuations do not exceed ±10%. Bakir and Kulaksiz in [34] used Genetic Algorithm (GA) and Bacterial Foraging Algorithm (BFA) to tune the STATCOM controller and obtained 30% and 20%

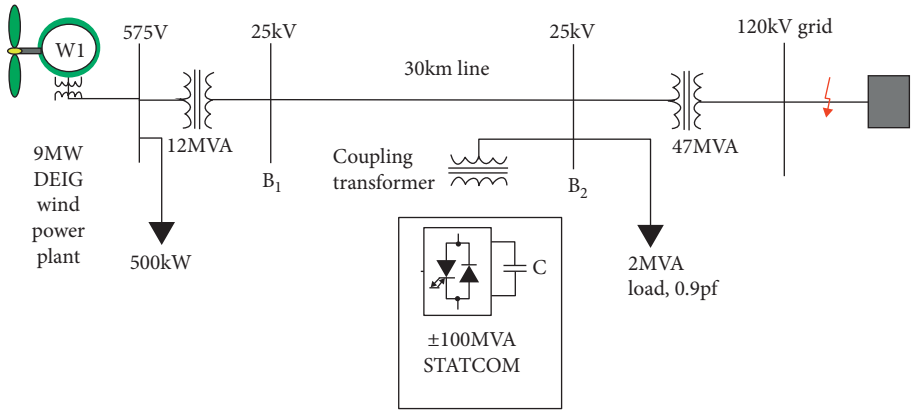

Figure 9: Single line diagram of test system [35].

Table 8: Transmission line parameters [19].

Transmission line parameters (π) model	
r_l	0.1153Ω/km
r_0	0.413Ω/km
l_l	0.00105 H/km
l_0	0.00332 H/km
C_l	$11.33e^{-9}$F/km
C_0	$5.01e^{-9}$F/km

voltage fluctuations, respectively, for *L-G* faults. Thus, the WCA and PSO tuned STATCOMs used in this work result in better results. Without a STATCOM, when the fault is cleared, the voltage rises momentarily to 1.12 p.u., due to the excess reactive power injected by the GSC during the fault period. Voltage fluctuations at the WPP terminals settle within 150 ms after fault clearance when a STATCOM is incorporated. Kamel et al. in [18] hybridized Ant Colony and Particle Swarm Optimization techniques and observed a settling time of 350 ms for a similar fault. Thus, WCA-PSO tuning results in a shorter settling time than ACO-PSO.

4.2.3. WPP Reactive Power Output. The reactive power output of the WPP for *L-G* 100% voltage sag of 150 ms on the grid side is shown in Figure 12.

From Figure 12, without a STATCOM, when the L-G grid fault occurs, the GSC injects up to 6 MVAr to support voltage at the WPP terminals. With STATCOM incorporation, GSC injects about 2 MVAr. With reactive power support, the PEC is not bypassed; thus, the DFIG generates active power during the grid fault. Reactive power oscillations are higher for conventional STATCOM as opposed to WCA-PSO tuned STATCOM.

4.2.4. DC Capacitor Link Voltage. DC capacitor link voltage of the DFIG WPP for *L-G* 100% voltage sag of 150 ms on the grid side is given in Figure 13.

From Figure 13, the DC link capacitor voltage fluctuates from a reference value of 1200 V to 1260 V and down to 1140 V (±5%) at the onset of the voltage sag. At the end of the fault period, the voltage rises to about 1280 V, when a STATCOM is not used. The voltage fluctuations are caused by excess reactive power injected by the GSC during the grid fault. When a STATCOM is used, the fluctuations are reduced since the GSC only injects minimum reactive power. The PSO tuned STATCOM results in the least fluctuations.

4.3. LLL-G Fault

4.3.1. WPP Active Power Output. The active power output of the WPP for LLL-G 100% grid voltage sag of 150 ms is given in Figure 14.

From Figure 14, during the LLL-G fault, the active power output at the WPP rapidly drops from about 8.8 MW up to 0 MW for the cases without, with conventional, and with PSO tuned STATCOM, due to the low voltage at the connection bus. The WPP gets disconnected and active power generation does not resume after fault clearance. LVRT capability requirement of German utility is not met for the three scenarios. For the case of WCA and WCA-PSO tuned models, the WPP rides through the LLL-G fault due to the voltage support provided at the PCC. Thus, the WPP stays online, but it does not generate active power. When the fault is cleared, active power generation quickly resumes to its prefault value.

4.3.2. Voltage Magnitude at WPP Terminals. The voltage profile at the WPP terminals is shown in Figure 15 for LLL-G 100% grid voltage sag of 150 ms.

From Figure 15, the voltage at the WPP terminal drops to 0 p.u. for cases without, with conventional, and with PSO tuned STATCOM, cases in which the WPP is disconnected. For WCA and WCA-PSO tuned STATCOM, the lowest voltage magnitude is 0.45 p.u. and 0.55 p.u., respectively. When the fault is cleared, there is an overvoltage due to reactive power supplied by the STATCOM during the fault period. The highest overshoot (30%) occurs with the WCA-PSO tuned STATCOM, which injects a maximum amount of reactive power, of 110 MVAr.

Table 9: Conventional STATCOM parameters [35].

S.No	Specifications	Quantity
1	Nominal voltage and frequency	500 $kV_{L\text{-}LRMS}$, 60 HZ
2	Converter rating	100 MAV
3	Converter impedance	$R_1 = 0.00733$ pu $L_{1=}0.22$ pu
4	DC link nominal voltage	40 kV
5	DC link nominal equivalent capacitance	$C = 3000\ \mu F$
6	Reference voltage	1 p.u
7	Droop	0.003 p.u
8	AC voltage regulator gains	$K_P = 5$ $K_1 = 1000$
9	DC voltage regulator gains	$K_P = 0.0001$ $K_1 = 0.02$
10	AC current regulator gains	$K_P = 0.3$ $K_1 = 10$

Table 10: PI controller gains.

STATCOM controller	Gain	Conventional STATCOM	PSO tuned FF = 0.2395 CT = 2052	WCA tuned FF = 0.2391 CT = 2007	WCA-PSO tuned FF = 0.238 CT = 2063
AC PI voltage regulator	K_{P1} K_{I1}	5 1000	5 1000	10 1200	8 1118
AC PI current regulator	K_{P2} K_{I2}	0.3 10	1 8	0.3 10	0.2 5
DC PI voltage regulator	K_{P3} K_{I3}	0.0001 0.02	0.001 0.01	0.09 0.01	0.001 0.05

FFFitness Function, CTComputation Time (sec).

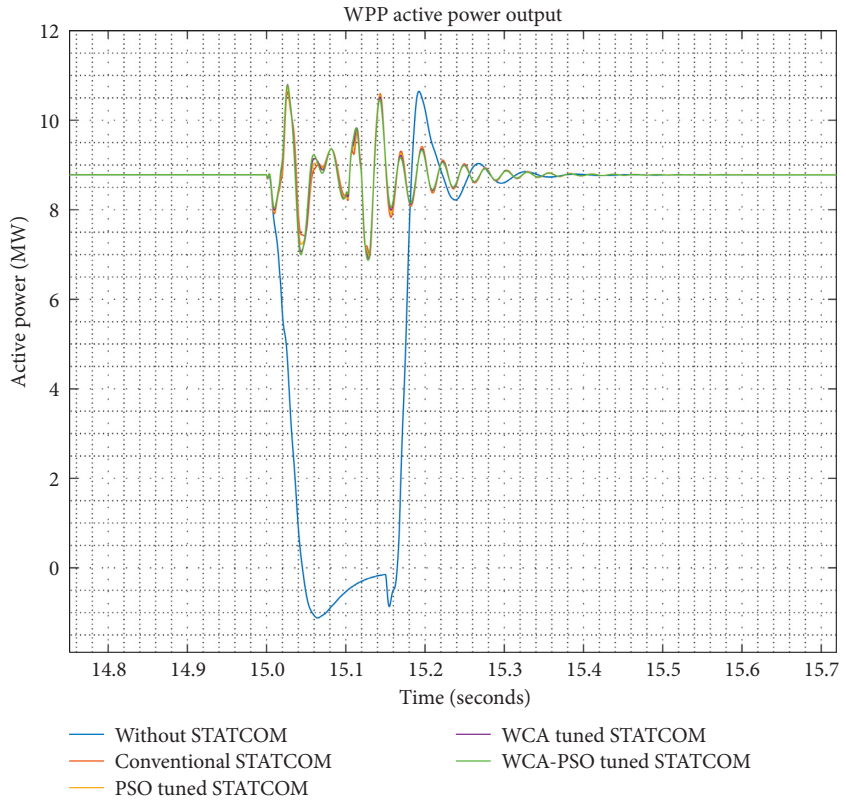

Figure 10: WPP active power output.

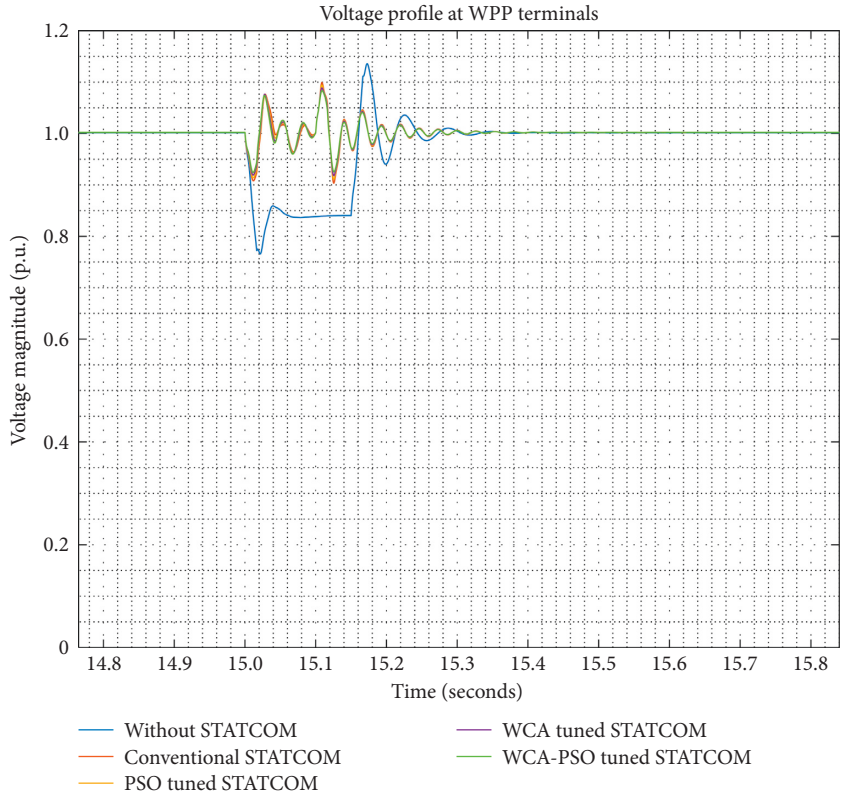

Figure 11: Voltage profile at WPP terminals.

4.3.3. WPP Reactive Power Output. Figure 16 shows the reactive power output of the WPP for LLL-G 100% grid voltage sags of 150 ms.

During the LLL-G grid fault, without STATCOM, the GSC injects up to 3.5 MVAr before WPP disconnection. For the WCA and WCA-PSO tuned STATCOM, the GSC injects 6.5 MVAr, to keep the WPP connected to the grid. The highest overshoots are seen for the WCA model, whereas WCA-PSO has a smoother output. For the WCA and WCA-PSO tuned STATCOMs, due to the excess reactive power after fault clearance, the GSC consumes reactive power up to −6.5 MVAr.

4.3.4. DC Capacitor Link Voltage. The DC link capacitor voltage of the DFIG WPP for LLL-G 100% grid voltage sag of 150 ms is shown in Figure 17.

From Figure 17, the DC link capacitor voltage of the DFIG under the LLL-G fault drastically increases from its steady-state value of 1200 V to a maximum of 1980 V when the WPP is disconnected. For the conventional and PSO tuned STATCOM, WPP disconnection is because the DC capacitor voltage limit of 1980 V is violated. The highest values of the DC capacitor link voltage for WCA and WCA-PSO tuned models are 1650 V and 1480 V, respectively, which are safe limits for the operation of the DC link capacitor.

4.3.5. Numerical Summary of Results. A comparison of voltage and current transient points at Bus 1 for the different tuning techniques is reported in Table 11.

From Table 11, PSO, WCA, and PSO-WCA tuned STATCOM utilization results in less voltage and current fluctuations at the point of wind power integration into the grid than the conventional PI method. The settling time is also shorter for tuned models, as compared to the conventional STATCOM. Kamel et al. in [18] made similar deductions on the impact of tuned STATCOM on voltage and current variations at the PCC and the settling time.

4.4. Analysis of Total Harmonic Distortion. Although harmonic problems are not as widespread as the RMS voltage fluctuations, harmonic distortion can negatively affect power system components. Harmonic effects include overheating of cables, transformers, and motors and interference in electronic and communication circuits. The Total Harmonic Distortion (THD) for voltage and currents at B_1 is summarized in Table 12 for the different algorithms.

From Table 12, PSO, WCA, and PSO-WCA tuned STATCOM utilization results in less THD of the voltage and current waveforms at the point of wind power injection into the grid, as compared to incorporating the conventional PI method. Kamel et al. in [18] made similar deductions on the effect of tuned STATCOM on THD.

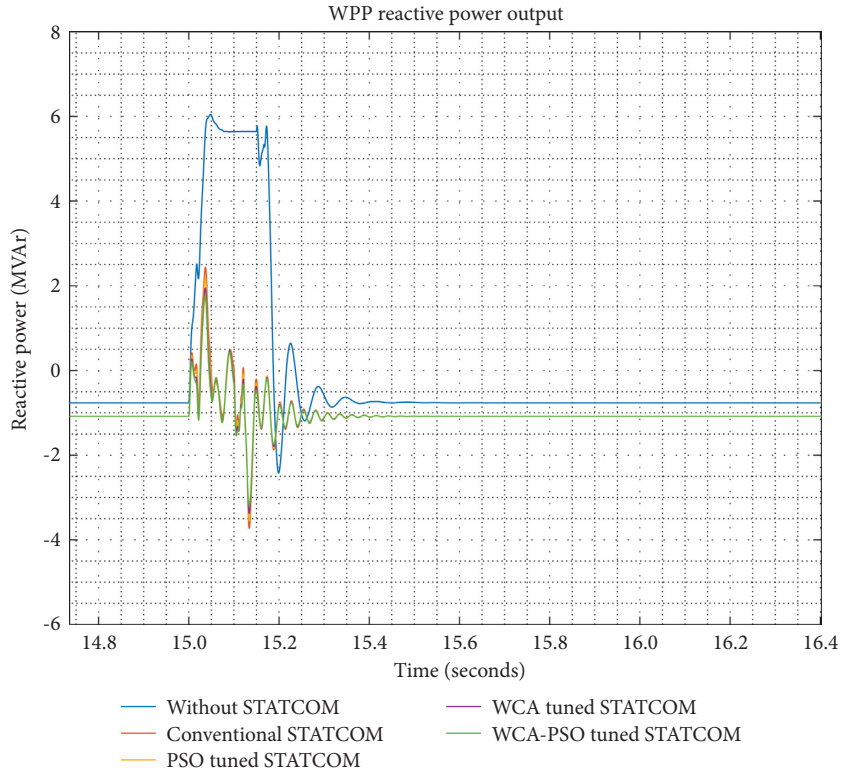

Figure 12: WPP reactive power output.

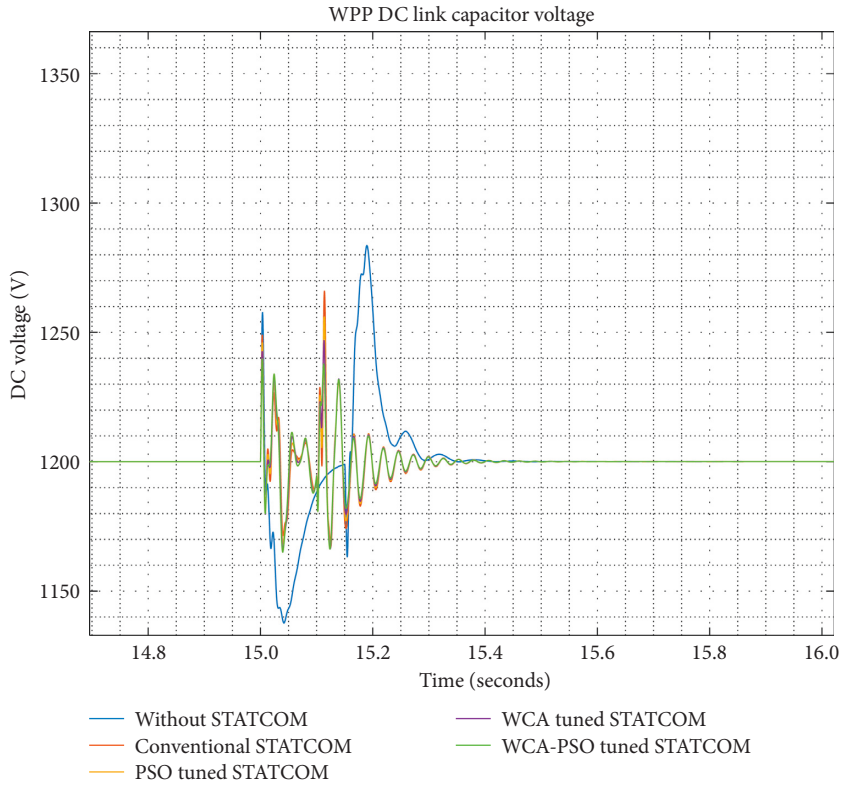

Figure 13: DC link capacitor voltage.

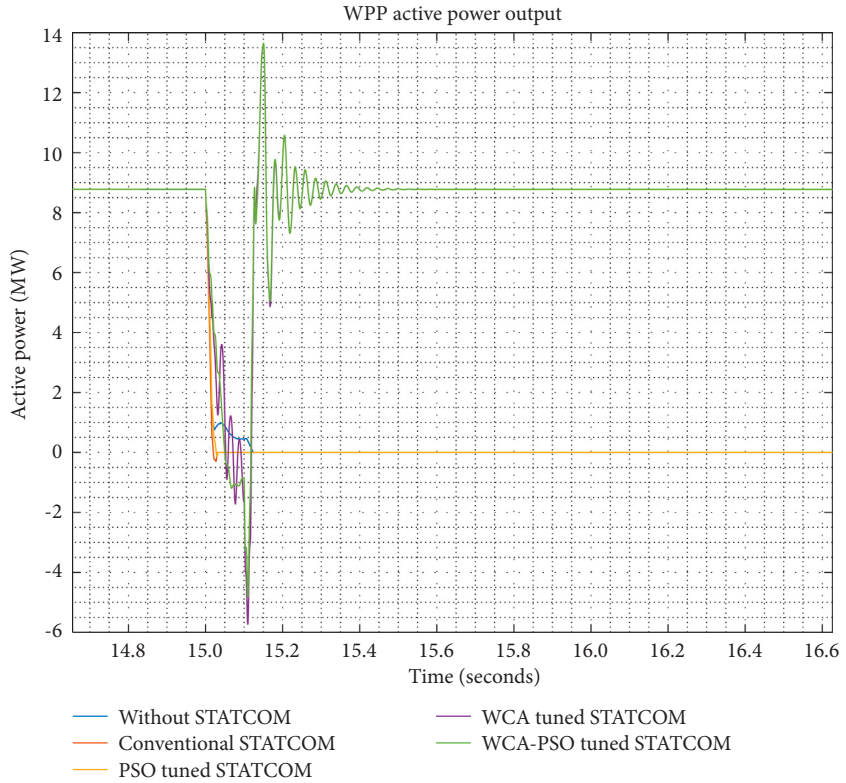

Figure 14: WPP active power output.

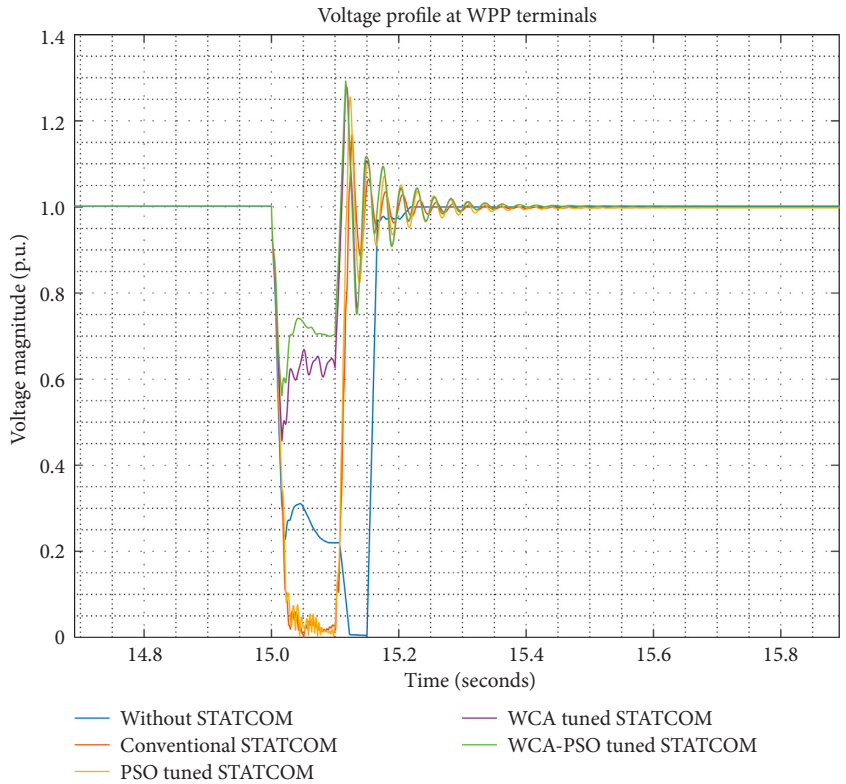

Figure 15: Voltage profile at WPP terminals.

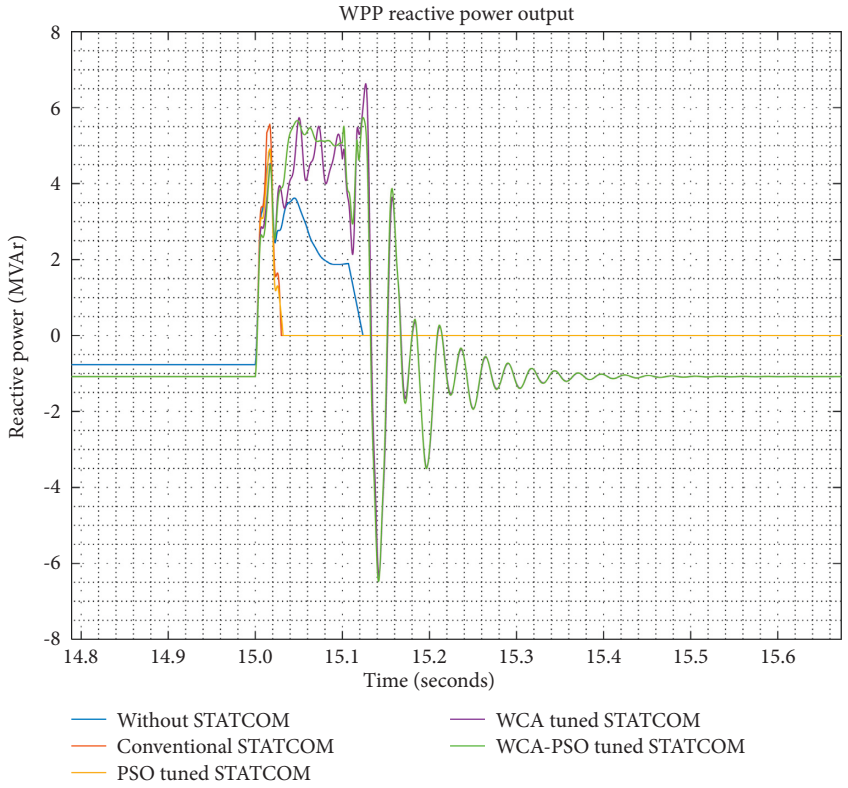

Figure 16: WPP reactive power output.

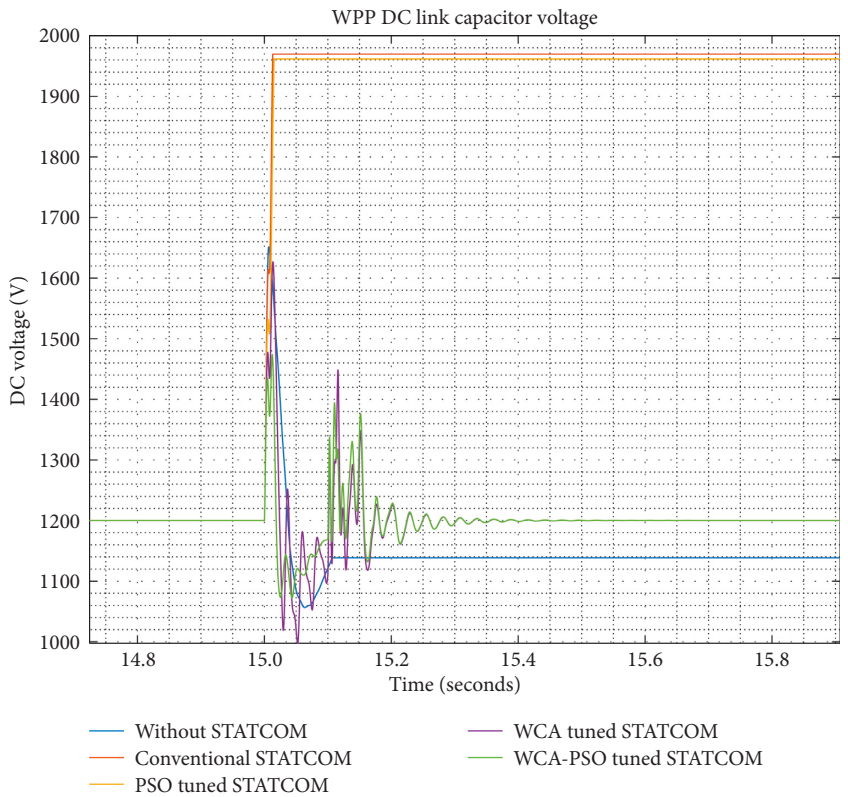

Figure 17: DC link capacitor voltage.

Table 11: Numerical summary of results obtained.

Fault type	Measured points	Transient points	Conventional STATCOM	PSO tuned STATCOM	WCA tuned STATCOM	WCA-PSO tuned STATCOM
L-G	V_{B1} (p.u.)	MOS	1.10	1.08	1.08	1.07
		MUS	0.90	0.92	0.92	0.90
		Ts(sec)	0.036	0.035	0.03	0.028
	I_{B1} (p.u.)	MOS	1.05	1.04	1.04	1.03
		MUS	0.75	0.80	0.80	0.82
		Ts(sec)	0.03	0.03	0.03	0.03
	V_{dc} (V)	MOS	1270	1265	1240	1230
		MUS	1170	1165	1165	1160
		Ts(sec)	0.037	0.035	0.035	0.03
LLL-G	V_{B1} (p.u.)	MOS	1.20	1.25	1.25	1.30
		MUS	0.00	0.00	0.40	0.50
		Ts(sec)	0.04	0.038	0.038	0.036
	I_{B1} (p.u.)	MOS	1.15	1.20	1.38	1.36
		MUS	0.00	0.00	0.20	0.30
		Ts(sec)	—	—	0.04	0.04
	V_{dc} (V)	MOS	1980	1960	1620	1480
		MUS	1200	1200	1000	1080
		Ts(sec)	—	—	0.35	0.35

MOSmaximum overshoot, MUSmaximum undershoot, *Ts*settling time.

Table 12: THD as a % of the fundamental value.

Parameter	Fault type	Conventional STATCOM (%)	PSO tuned STATCOM (%)	WCA tuned STATCOM (%)	WCA-PSO tuned STATCOM (%)
V_{abc} (B_1)	*L-G*	5.66	4.8	4.62	3.92
	LLL-G	8.85	8.44	8.33	7.76
I_{abc} (B_1)	*L-G*	24.54	11.67	11.93	8.84
	LLL-G	2.26	1.53	1.72	1.24

Table 13: Generator data [55].

Generator no.	Bus no.	Active power generated (MW)	Reactive power generated (MVAr)	Q_{max} (MVAr)	Q_{min} (MVAr)	Generator voltage	P_{max} (MW)	P_{min} (MW)
1	30	250.00	161.76	400	140	1.05	1040	0
2	31	677.87	221.57	300	−100	0.98	646	0
3	32	650.00	206.97	300	150	0.98	725	0
4	33	632.00	108.29	250	0	1.00	652	0
5	34	508.00	166.69	167	0	1.01	508	0
6	35	650.00	210.66	300	−100	1.05	687	0
7	36	560.00	100.17	240	0	1.06	580	0
8	37	540.00	−1.37	250	0	1.03	564	0
9	38	830.00	21.73	300	−150	1.03	865	0
10	39	1000.00	78.47	300	−100	1.03	1100	0
Total		6297.87					7367	

4.5. IEEE 39 Bus Test System. The IEEE 39 bus test system is a simplified model of the high voltage transmission system in the northeast of the USA (New England area), which consists of 10 generators, 19 loads, 34 lines, and 12 transformers. The test system data generator, bus, and transmission line data is given in Tables 13–15, respectively. The online diagram of the modified IEEE 39 bus test system is shown in Figure 18 [48].

The aggregate capacity of the IEEE 39-bus system is 6140.80 MW while the total connected load is 6097.1 MW. Bus number 39 is taken as the slack bus. All generators in this standard system are modeled as 4^{th}-order synchronous machines equipped with standard IEEE models of automatic voltage regulators, excitation systems, governor systems, and power system stabilizers.

Elzemeity et al. in [49] investigate the optimal location of WPPs in the IEEE 39 bus system by sorting the possible locations in ascending order of electromechanical oscillations using Eigenvalue analysis. The best five locations with less electromechanical oscillations are obtained as

Table 14: Bus data [55].

Bus no.	Active power load (MW)	Reactive power load (MVAr)
1	97.60	44.20
2	0.00	0.00
3	322.00	2.40
4	500.00	184.00
5	0.00	0.00
6	0.00	0.00
7	233.80	84.00
8	522.00	176.60
9	6.50	−66.60
10	0.00	0.00
11	0.00	0.00
12	8.53	88.00
13	0.00	0.00
14	0.00	0.00
15	320.00	153.00
16	329.00	32.30
17	0.00	0.00
18	158.00	30.00
19	0.00	0.00
20	680.00	103.00
21	274.00	115.00
22	0.00	0.00
23	247.50	84.60
24	308.60	-92.20
25	224.00	47.20
26	139.00	17.00
27	281.00	75.50
28	206.00	27.60
29	283.50	26.90
30	0.00	0.00
31	9.20	4.60
32	0.00	0.00
33	0.00	0.00
34	0.00	0.00
35	0.00	0.00
36	0.00	0.00
37	0.00	0.00
38	0.00	0.00
39	1104.00	250.00
Total	6254.23	1387.10

Table 15: Transmission line data [55].

Line no.	From bus	To bus	R (p.u.)	X (p.u.)	B (p.u.)	Ratio
1	1	2	0.0035	0.0411	0.6987	0
2	1	39	0.0010	0.0250	0.7500	0
3	2	3	0.0013	0.0151	0.2572	0
4	2	25	0.0070	0.0086	0.1460	0
5	2	30	0.0000	0.0181	0.0000	1.025
6	3	4	0.0013	0.0213	0.2214	0
7	3	18	0.0011	0.0133	0.2138	0
8	4	5	0.0008	0.0128	0.1342	0
9	4	14	0.0008	0.0129	0.1382	0
10	5	6	0.0002	0.0026	0.0434	0
11	5	8	0.0008	0.0112	0.1476	0
12	6	7	0.0006	0.0092	0.1130	0
13	6	11	0.0007	0.0082	0.1389	0
14	6	31	0.0000	0.0250	0.0000	1.07
15	7	8	0.0004	0.0046	0.0780	0
16	8	9	0.0023	0.0363	0.3804	0
17	9	39	0.0010	0.0250	1.2000	0
18	10	11	0.0004	0.0043	0.0729	0
19	10	13	0.0004	0.0043	0.0729	0
20	10	32	0.0000	0.0200	0.0000	1.07
21	12	11	0.0016	0.0435	0.0000	1.006
22	12	13	0.0016	0.0435	0.0000	1.006
23	13	14	0.0009	0.0101	0.1723	0
24	14	15	0.0018	0.0217	0.3660	0
25	15	16	0.0009	0.0094	0.1710	0
26	16	17	0.0007	0.0089	0.1342	0
27	16	19	0.0016	0.0195	0.3040	0
28	16	21	0.0008	0.0135	0.2548	0
29	16	24	0.0003	0.0059	0.0680	0
30	17	18	0.0007	0.0082	0.1319	0
31	17	27	0.0013	0.0173	0.3216	0
32	19	20	0.0007	0.0138	0.0000	1.06
33	19	33	0.0007	0.0142	0.0000	1.07
34	20	34	0.0009	0.0180	0.0000	1.009
35	21	22	0.0008	0.0140	0.2565	0
36	22	23	0.0006	0.0096	0.1846	0
37	22	35	0.0000	0.0143	0.0000	1.025
38	23	24	0.0022	0.0350	0.3610	0
39	23	36	0.0005	0.0272	0.0000	1
40	25	26	0.0032	0.0323	0.5310	0
41	25	37	0.0006	0.0232	0.0000	1.025
42	26	27	0.0014	0.0147	0.2396	0
43	26	28	0.0043	0.0474	0.7802	0
44	26	29	0.0057	0.0625	1.0290	0
45	28	29	0.0014	0.0151	0.2490	0
46	29	38	0.0008	0.0156	0.0000	1.025

buses 30, 37, 31, 32, and 36, respectively. These findings agree with Essalah et al. in [50] in which buses 30, 34, 37, and 39 are obtained as the optimal location for WPPs, and Shi et al. in [51] who obtain optimal locations as buses 38 and 37. El-Samanoudy et al. in [52] also assess the impact of large-scale wind generation on the IEEE 39 bus system based on voltage stability and conclude that the integrated wind power generation should not exceed 20% for system stability.

In this work, the synchronous generators in bus 30 and bus 37 were replaced with the same amount of active power generation, and reactive power needs were met by installing capacitors. This ensured the same system operating conditions were maintained. The 250 MW, 162 MVAr (bus 30) and 540 MW, −1.4 MVAr (bus 37) synchronous generators were replaced by wind farms equipped with GE 1.5 MW DFIG generators. The penetration level of wind power generation is therefore 12%. Two STATCOMs are also integrated at the point of wind power integration into the grid. Similarly, the STATCOMs are tuned using WCA, PSO, and WCA-PSO optimization algorithms. To investigate the LVRT capability of the WPPs, the LLL-G fault was simulated online 16–17. This fault location has been identified by Arredondo et al. in [53] and Yakout et al. in [54], as the most severe line loss which can lead to transient stability. The IEEE 39 bus test system was thus subjected to LLL-G, online 16–17 for 150 ms, to evaluate the German electric utility LVRT capability requirement. The assumptions for wind speed, simulation time, and crowbar configuration are the same as in the 9 MW test system.

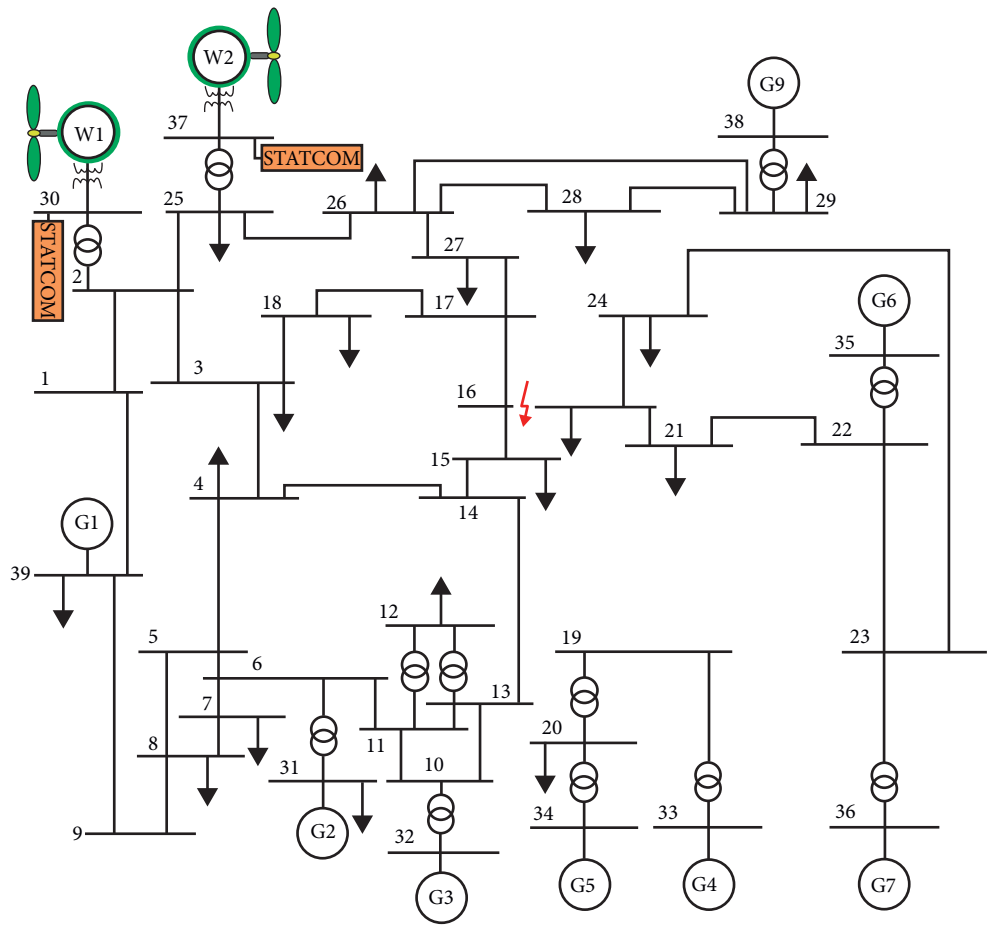

Figure 18: IEEE 39 bus test system [49].

4.6. LLL-G Fault

4.6.1. WPP Active Power Output. The active power output of the 250 MW (WPP 1) for the LLL-G grid fault of 150 ms is given in Figure 19.

From Figure 19, during the LLL-G fault, the active power output of WPP 1 rapidly drops from about 245 MW up to −35 MW for the cases without a STATCOM, with conventional and with PSO tuned STATCOM. For the WCA tuned STATCOM, the lowest output is −20 MW whereas for WCA-PSO tuned STATCOM, the lowest output is 20 MW. For all the scenarios, the WPP stays online, although it only generates active power when WCA-PSO tuned STATCOM is incorporated. The WCA-PSO tuned STATCOM gives the best outcome, in which it injects maximum reactive power of 110 MVAr, and the GSC regulates active power generation. The WPP thus rides through the LLL-G fault due to the voltage support provided at the PCC for all scenarios. When the fault is cleared, active power generation quickly recovers to its prefault value. The active power output of the 540 MW (WPP 2) is given in Figure 20, in which the WPP can ride through the LLL-G fault in all scenarios.

4.6.2. Voltage Magnitude at WPP 1 Terminals. The voltage profile at WPP 1 terminals is shown in Figure 21 for the LLL-G grid fault of 150 ms.

From Figure 21, for WPP 1 at bus 30, some voltage fluctuations are observed. Voltage magnitude drops from 1 p.u. to 0.88 p.u. without STATCOM, whereas for the tuned models, the lowest voltage magnitude is 0.94 p.u. Voltage fluctuations are minimum at the WPP terminals during, and after fault clearance for WCA-PSO tuned STATCOM. The voltage profile at the terminals of WPP 2 at bus 37 is given in Figure 22.

For the second WPP, voltage fluctuations during the LLL-G fault are minimal, and the WPP rides through the grid fault. The WCA-PSO tuned STATCOM scenario has a better profile.

4.6.3. WPP Reactive Power Output. The reactive power output of WPP 1 for LLL-G grid fault of 150 ms is given in Figure 23.

The GSC injects reactive power, to aid grid recovery. The highest transients are seen for the WCA model, whereas WCA-PSO has a smoother output.

From Figure 24, without a STATCOM, when the LLL-G grid fault occurs, the GSC injects up to 350 MVAr to support voltage at the WPP terminals. With STATCOM incorporation, GSC injects less reactive power, with the least amount of reactive injected for WCA-PSO tuned STATCOM, 170 MVAr. The WPP stays online, thus the DFIG generates active power during the grid fault. Reactive power

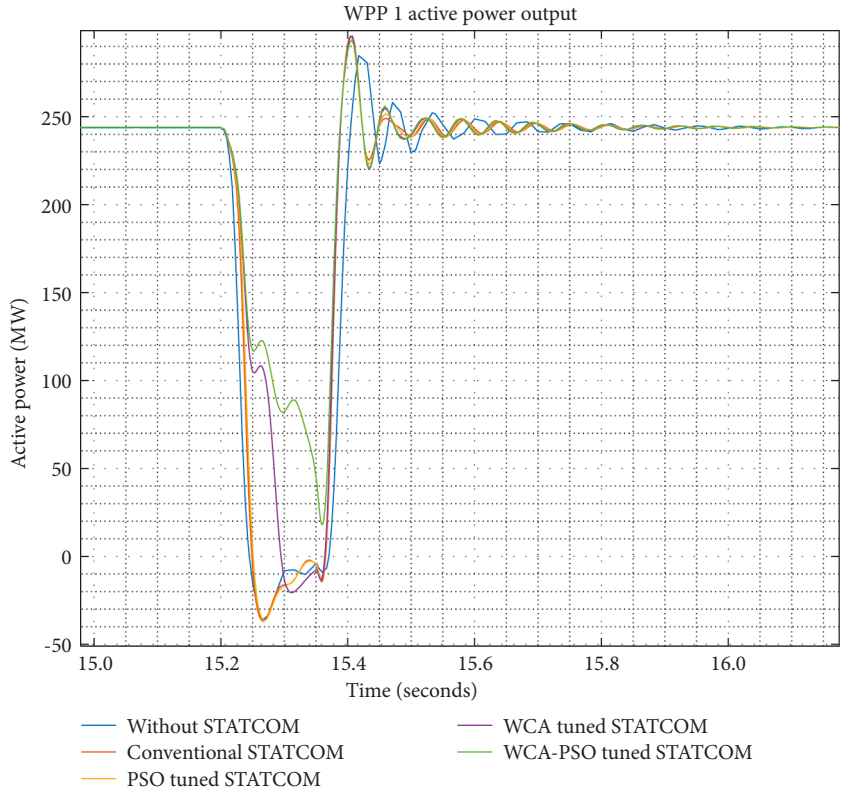

Figure 19: WPP 1 active power output.

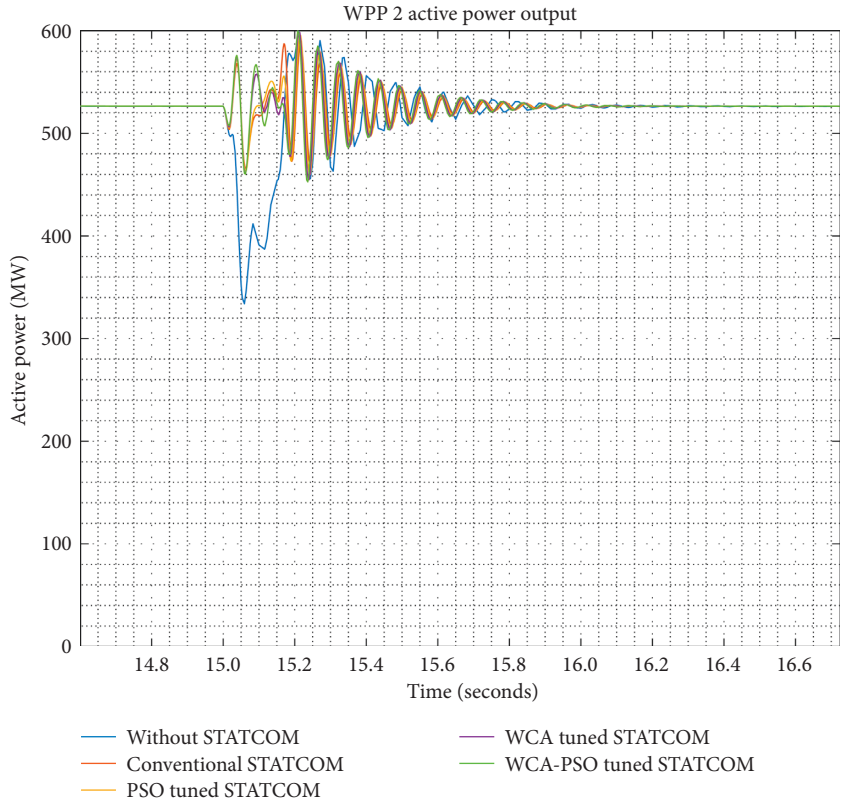

Figure 20: WPP 2 active power output.

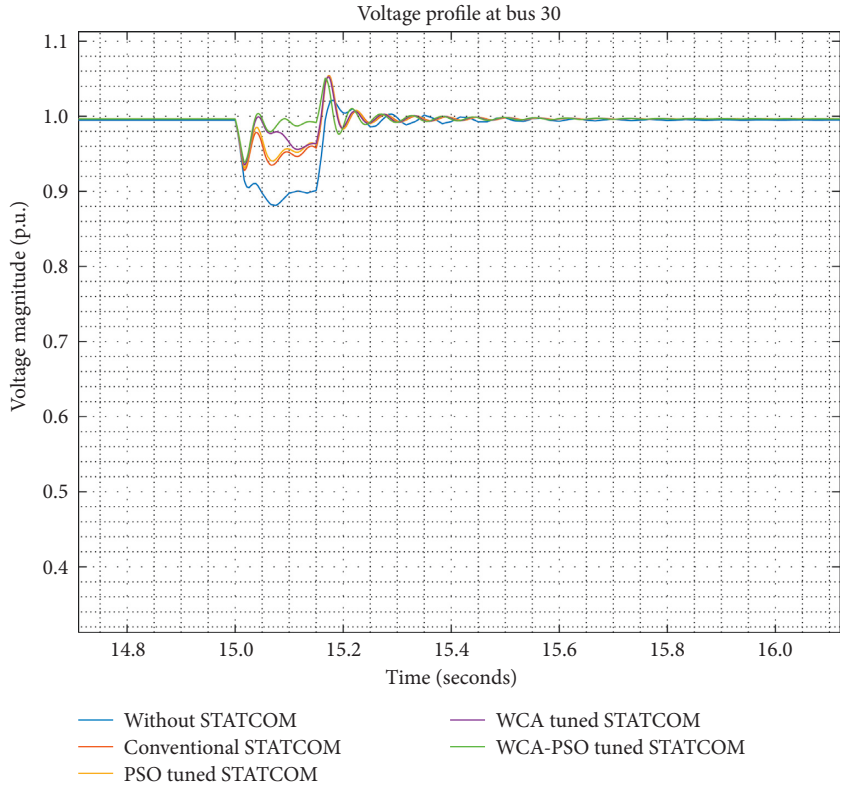

Figure 21: Voltage profile at WPP terminals.

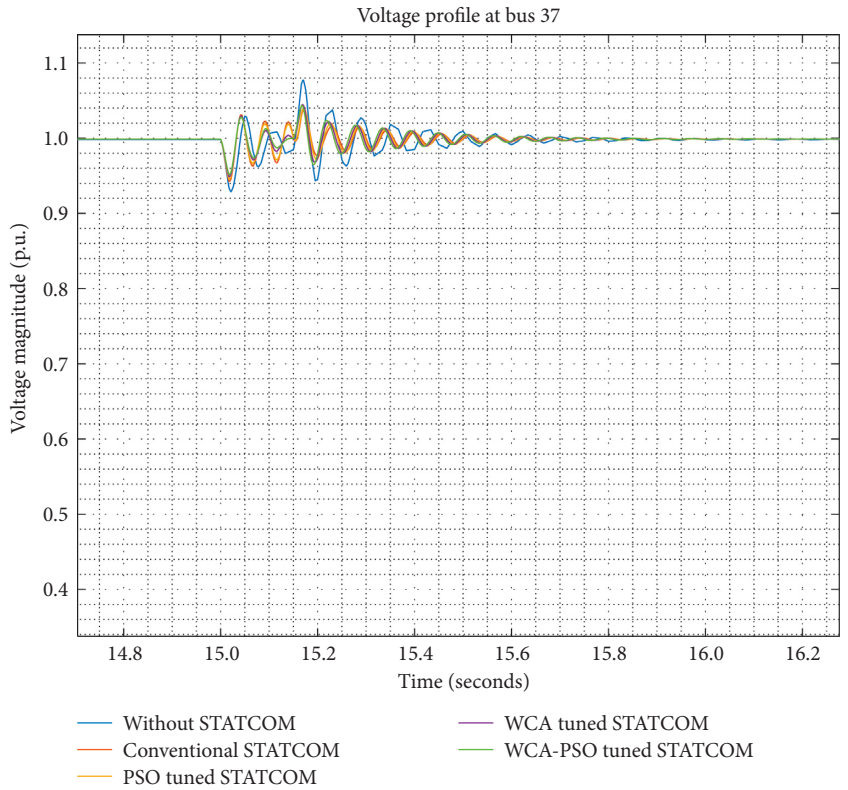

Figure 22: Voltage profile at WPP terminals.

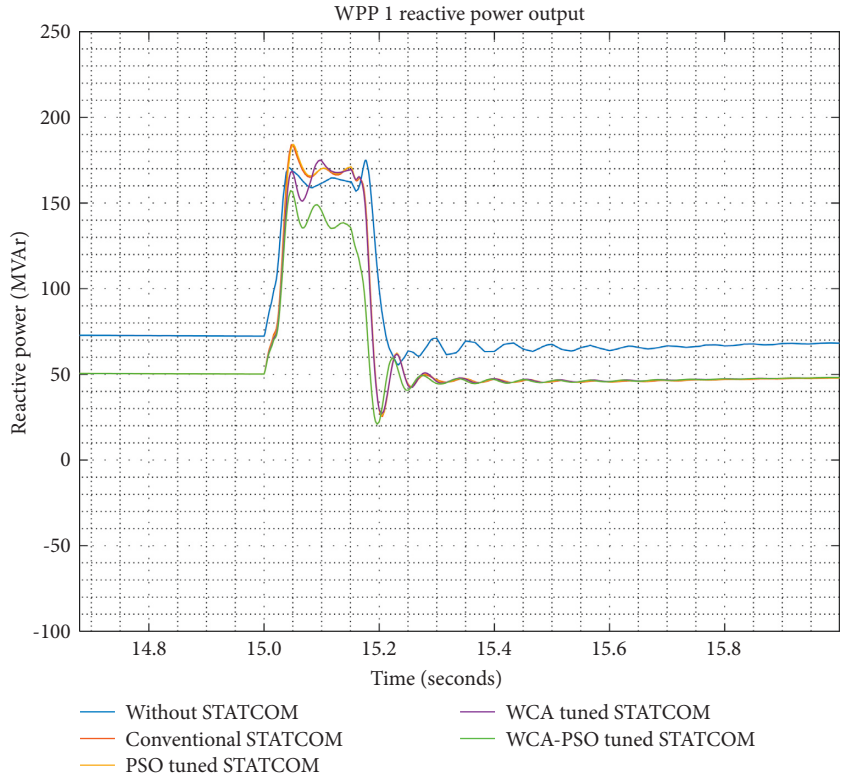

Figure 23: WPP 1 reactive power output.

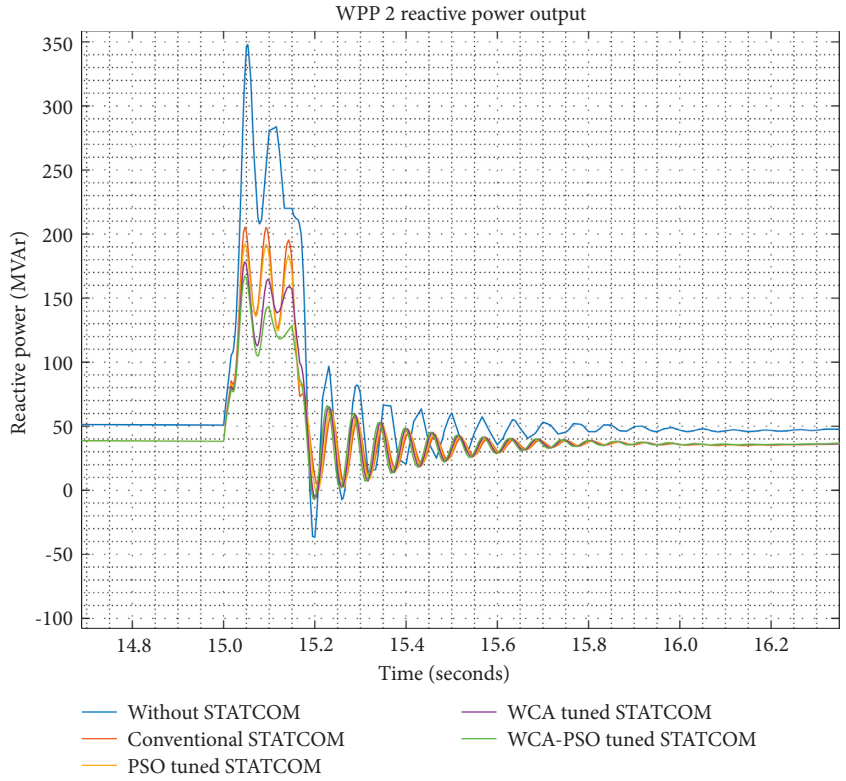

Figure 24: WPP 2 reactive power output.

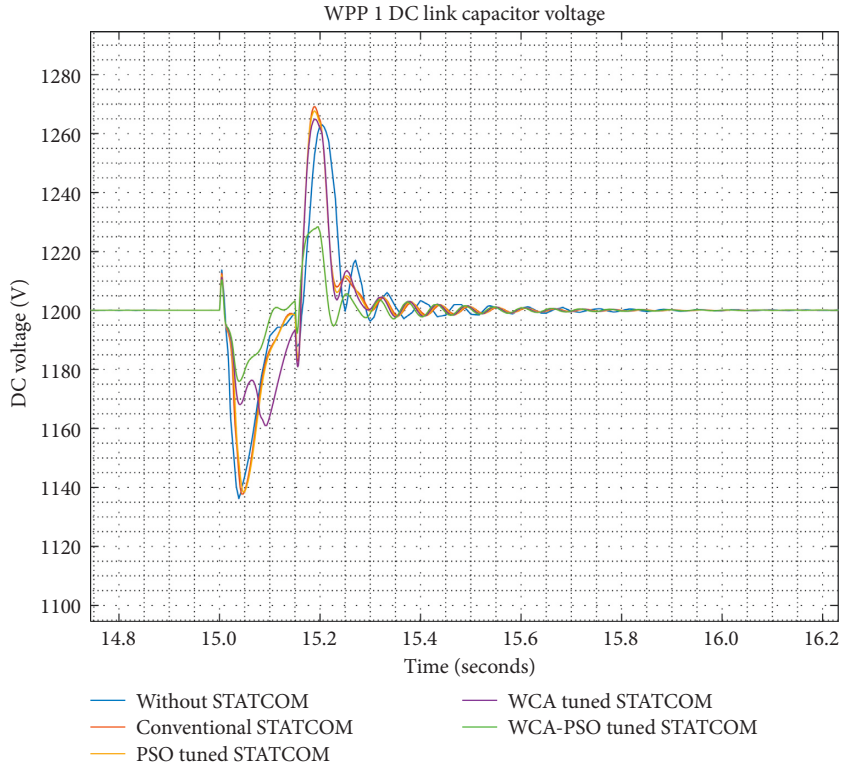

Figure 25: WPP 1 DC link capacitor voltage.

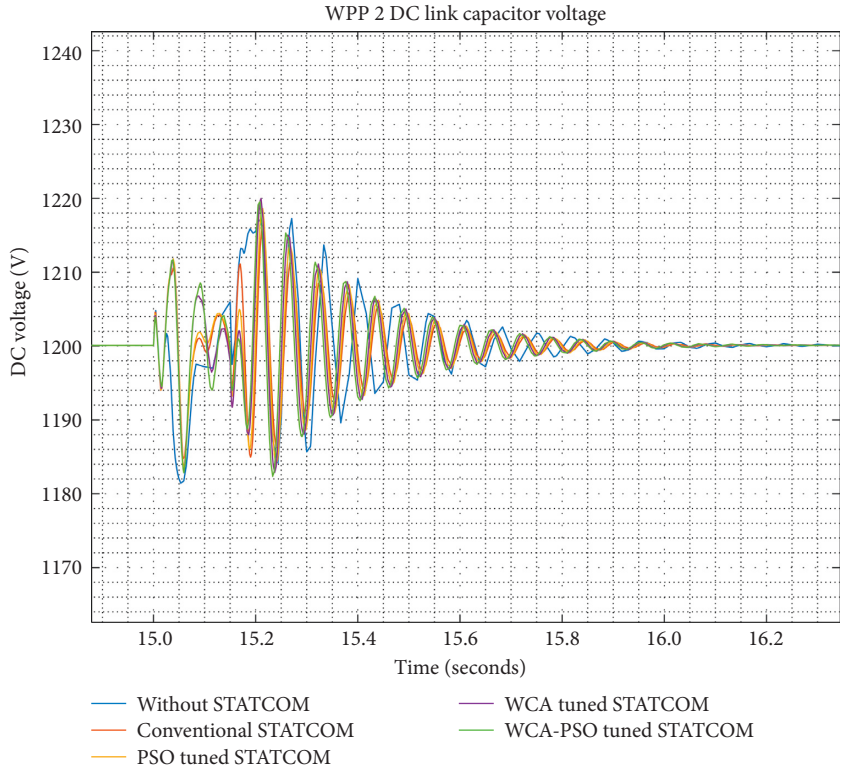

Figure 26: WPP 2 DC link capacitor voltage.

oscillations are higher for conventional STATCOM as opposed to WCA-PSO tuned STATCOM.

4.6.4. DC Capacitor Link Voltage. The DC link capacitor voltage of the DFIG in 250 MW WPP for LLL-G grid fault of 150 ms is shown in Figure 25.

From Figure 25, the DC link capacitor voltage fluctuates from a reference value of 1200 V to around 1135 V at the onset of the voltage sag and back to about 1270 V at the end of the fault period, when a STATCOM is not used. The WCA-PSO tuned STATCOM results in the least fluctuations. The DC capacitor voltage for WPP 2 is shown in Figure 26 in which the fluctuations are about ±2%, which is within a safe operating range.

5. Conclusion

In this paper, the LVRT capability of grid-connected DFIG-based WPPs is investigated against requirements for the German utility grid. The STATCOM has been used for reactive power compensation to enhance LVRT capability and improve the dynamic performance of grid-connected WPPs. STATCOM controller tuning has been done using WCA, PSO, and WCA-PSO hybrid algorithms. The WCA is a recent optimizer which has not been previously employed in power system applications such as controller tuning. The validity of the proposed STATCOM controller tuning approach was verified during *L-G* and LLL-G grid faults for 150 ms. Simulations were conducted in MATLAB programming language using the SimScape toolbox, for the 9 MW WPP test system and the IEEE 39 bus test system. Performance comparison was done for conventional, WCA, PSO, and WCA-PSO tuned STATCOM, in terms of voltage profiles, active and reactive power, under *L-G* and LLL-G faults independently. For the 9 MW test system, the LVRT capability of the German power system was met for *L-G* faults. During the *L-G* fault, voltage magnitude drops from 1 p.u. to 0.76 p.u. without STATCOM, whereas for the tuned models, the lowest voltage magnitude is 0.9 p.u. During LLL-G faults, without, with conventional, and with PSO tuned STATCOMs, the WPP could not ride through the fault. When WCA and WCA-PSO tuned STATCOM was incorporated, the German LVRT capability requirement for the 9 MW test system was met. During the LLL-G fault, the voltage at the WPP terminal drops to 0 p.u. for cases without, with conventional, and with PSO tuned STATCOM, whereas WCA and WCA-PSO tuned STATCOM have the lowest voltage magnitude of 0.45 p.u. and 0.55 p.u., respectively. The two WPPs installed in the IEEE 39 bus test system were able to ride through the LLL-G grid fault. Voltage magnitude drops from 1 p.u. to 0.88 p.u. without STATCOM, while for the tuned models, the lowest voltage magnitude is 0.94 p.u. In all test scenarios, WCA-PSO tuned STATCOM utilization resulted in less voltage and active and reactive power overshoots. However, transients were observed at the beginning and end of the fault period. Since the STATCOM provides reactive power support, an additional technique of limiting the fault current can be incorporated, such as the FCL, SDBR, or a DC chopper, thus ensuring that the WPP meets LVRT capability requirements during LLL-G faults. The proposed tuned STATCOM can also be investigated in the enhancement of LVRT GCRs for other utility grids such as Denmark, the USA, or any other country, as given in Table 1. WCA-PSO algorithm can further be applied in various power system optimization problems. STATCOM controller tuning using other metaheuristic optimization algorithms should be explored further and evaluated on larger practical power systems, under different grid faults.

Abbreviations and Symbols

DFIG: Doubly Fed Induction Generator
FACTS: Flexible AC Transmission System
GCR: Grid Code Requirement
GSC: Grid Side Converter
LVRT: Low Voltage Ride Through
PI: Proportional and integral control
PSO: Particle Swarm Optimization
RSC: Rotor Side Converter
STATCOM: Static Compensator
VAr: Reactive power
VSI: Voltage Source Inverter
WCA: Water Cycle Algorithm
WRIG: Wound rotor induction generator
WTG: Wind Turbine Generator
A_r: Area swept by rotor blades
β: Blade pitch angle
C_p: Power coefficient
L_s: Stator inductance
L_r: Rotor inductance
$L_{s\sigma}$: Stator leakage
$L_{r\sigma}$: Rotor self-inductance
L_m: Mutual inductance
R: Resistance
Ψ: Flux linkage
λ: Tip-Speed Ratio
ρ: Air density
v_w: Wind speed
ω_e: Supply angular frequency
ω_r: Rotor angular frequency.

Appendix

AConventional STATCOM Parameters

Conventional STATCOM Parameters are shown in Table 9.

B9 MW Test System Data

Wind turbine parameters, wind generator parameters, and transmission line parameters are shown in Tables 6–8, respectively.

CIEEE 39 Bus Test System

Generator data, bus data, and transmission line data are shown in Tables 13–15, respectively.

Data Availability

All relevant data are in the appendix of the article.

Conflicts of Interest

The authors declare that there are no conflicts of interest regarding the publication of this article.

Acknowledgments

This work was supported by Pan African University Institute for Basic Sciences, Technology and Innovation.

References

[1] O. Kamel, A. Abdelaziz, and A. Diab, "Damping oscillation techniques for wind farm DFIG integrated into inter-connected power system," *Electric Power Components and Systems*, vol. 0, no. 0, pp. 1–20, 2021.

[2] Irena, *Renewable Capacity Statistics*, International Renewable Energy Agency, Abu Dhabi, 2020.

[3] A. M. Ibrahim, S. A. Gawish, N. H. El-Amary, and S. M. Sharaf, "STATCOM controller design and experimental investigation for wind generation system," *IEEE Access*, vol. 7, Article ID 150453, 2019.

[4] D. Chauhan and S. Goel, "Designing of advanced crowbar protection system for DFIG coupled wind energy conversion system at different fault conditions," *International Journal of Science Technology & Engineering*, vol. 4, no. 11, pp. 119–125, 2018.

[5] S. Soued, H. S. Ramadan, and M. Becherif, "Effect of doubly fed induction generator on transient stability analysis under fault conditions," *Energy Procedia*, vol. 162, pp. 315–324, 2019.

[6] D. Bhutto, J. Ansari, and H. Bukhari, "Wind energy conversion systems (WECS) generators: a review," in *Proceedings of the International Conference on Computing, Mathematics and Engineering Technologies*, Sukkur, Pakistan, January 2019.

[7] Y. Peng, Y. Li, Z. Xu et al., "Power quality improvement and LVRT capability enhancement of wind farms by means of an inductive filtering method," *Energies*, vol. 9, p. 302, 2016.

[8] H. Rezaie and M. H. Kazemi-Rahbar, "Enhancing voltage stability and LVRT capability of a wind-integrated power system using a fuzzy-based SVC," *Engineering Science and Technology, an International Journal*, vol. 22, no. 3, pp. 827–839, 2019.

[9] Y.-L. Hu, Y.-K. Wu, C.-K. Chen et al., "A review of the low-voltage ride-through capability of wind power generators," *Energy Procedia*, vol. 141, pp. 378–382, 2017.

[10] R. A. Jerin, P. Kaliannan, U. Subramaniam, and M. El-Moursi, "A review on Fault Ride through solutions for improving transient stability in DFIG based wind turbines," *IET Renewable Power Generation*, vol. 12, pp. 1–25, 2018.

[11] Y. Qu, L. Gao, G. Ma, H. Song, and S. Wang, "Crowbar resistance value-switching scheme conjoint analysis based on statistical sampling for LVRT of DFIG," *Journal of Modern Power Systems and Clean Energy*, vol. 7, no. 3, pp. 558–567, 2019.

[12] B. Qin, H. Li, X. Zhou, J. Li, and W. Liu, "Low-voltage ride-through techniques in DFIG-BasedWind turbines: a review," *Applied Sciences*, vol. 10, no. 2154, pp. 1–25, 2020.

[13] A. Parameswari and H. Sait, "A comprehensive review of fault ride-through capability of wind turbines with grid-connected doubly fed induction generator," *International Transactions on Electrical Energy Systems*, vol. etep12395, 2020.

[14] S. Divya and T. Krishnakumari, "Review of control strategies for DFIG wind turbine to enhance LVRT Capability," *International Journal of Innovative Science, Engineering & Technology*, vol. 2, no. 4, pp. 339–343, 2015.

[15] P. D. Chung, "Voltage enhancement on DFIG based wind farm terminal during grid faults," *Engineering, Technology & Applied Science Research*, vol. 9, no. 5, pp. 4783–4788, 2019.

[16] D. Zhang, H. Xu, L. Qiao, and L. Chen, "LVRT capability enhancement of DFIG based wind turbine with coordination control of Dynamic Voltage Restorer and inductive Fault Current Limiter," *PLoS One*, vol. 14, no. 8, Article ID e0221410, 2019.

[17] A. Rashad, S. Kamel, F. Jurado, M. Nasser, and K. Mahmoud, "ANN-based STATCOM tuning for performance enhancement of combined wind farms," *Electric Power Components and Systems*, pp. 1–17, 2019.

[18] O. M. Kamel, A. A. Z. Diab, T. D. Do, and M. A. Mossa, "A novel hybrid Ant colony-particle swarm optimization techniques based tuning STATCOM for grid code compliance," *IEEE Access*, vol. 8, Article ID 41566, 2020.

[19] A. Benali, M. Khiat, T. Allaoui, and M. Denai, "Power quality improvement and low voltage ride through capability in hybrid wind-PV farms grid-connected using dynamic voltage restorer," *IEEE Access*, vol. 6, no. 1, Article ID 68634, 2018.

[20] R. A. Jerin, P. Kaliannan, U. Subramaniam, and A. Thirumoorthy, "Power quality improvement of grid connected wind farms through voltage restoration using dynamic voltage restorer," *International Journal of Renewable Energy Resources*, vol. 6, no. 1, 2016.

[21] S. Kumar, A. Rahman, and R. Ahmed, "Tuning of PI and PID controller with STATCOM, SSSC and UPFC for minimizing damping of oscillation," *IOSR Journal of Electrical and Electronics Engineering*, vol. 12, no. 1, pp. 30–44, 2017.

[22] H. Wu, W. Su, and Z. Liu, "PID controllers: design and tuning methods," in *Proceedings of the IEEE Conference on Industrial Electronics and Applications*, Hangzhou, China, June 2014.

[23] Y.-Y. Hong, M.-T. Nguyen, and H. Zeng, "Studies on optimal controller design of STATCOM in power system with large wind farms," in *Proceedings of the International Conference on Electrical Engineering*, Korea, June 2018.

[24] O. Noureldeen and I. Hamdan, "A novel controllable crowbar based on fault type protection technique for DFIG wind energy conversion system using adaptive neuro-fuzzy inference system," *Protection and Control of Modern Power Systems*, vol. 3, no. 35, pp. 1–12, 2018.

[25] S. Zain and I. A. Ahmed Helal, "Low voltage ride through capability techniques for DFIG-based wind turbines," *International Journal of Energy and Power Engineering*, vol. 10, no. 7, pp. 910–919, 2016.

[26] R. Ann, P. Kaliannan, S. Padmanaban, and V. Ramachandaramurthy, "Improved Fault Ride through capability in DFIG based wind turbines using dynamic voltage restorer with combined feed-forward and feed-back control," *IEEE Access*, vol. 5, Article ID 20494, 2017.

[27] J. Mwaniki, H. Lin, and Z. Dai, "A concise presentation of doubly fed induction generator wind energy conversion systems challenges and solutions," *Journal of Engineering*, vol. 2017, pp. 1–13, Article ID 4015102, 2017.

[28] I. Hamdan, A. Ibrahim, and O. Noureldeen, "Modified STATCOM control strategy for fault ride-through capability enhancement of grid-connected PV/wind hybrid power

system during voltage sag," *SN Applied Sciences*, vol. 2, no. 364, 2020.

[29] J. J. Justo, F. Mwasilu, and J.-W. Jung, "Doubly-fed induction generator based wind turbines: a comprehensive review of fault ride-through strategies," *Renewable and Sustainable Energy Reviews*, vol. 45, pp. 447–467, 2015.

[30] O. P. Mahela, N. Gupta, M. Khosravy, and N. Patel, "Comprehensive overview of low voltage ride through methods of grid integrated wind generator," *IEEE Access*, vol. 7, Article ID 99299, 2019.

[31] L. Yuan, K. Meng, J. Huang, Z. Dong, W. Zhang, and X. Xie, "Development of HVRT and LVRT control strategy for PMSG-based wind turbine generators," *Energies*, vol. 13, no. 5442, pp. 1–16, 2020.

[32] A. A. AbdElhafez, S. H. Alruways, Y. A. Alsaif, M. F. Althobaiti, A. B. Alotaibi, and N. A. Alotaibi, "Reactive power problem and solutions: an overview," *Journal of Power and Energy Engineering*, vol. 05, no. 05, pp. 40–54, 2017.

[33] S. Juna, K. Akhtar, and S. Peng, "Improving power quality and stability of wind energy conversion system with fuzzy-controlled STATCOM," *Australian Journal of Electrical and Electronics Engineering*, pp. 1–10, 2015.

[34] H. Bakir and A. A. Kulaksiz, "Modelling and voltage control of the solar-wind hybrid micro-grid with optimized STATCOM using GA and BFA," *Engineering Science and Technology, an International Journal*, vol. 23, no. 3, pp. 576–584, 2020.

[35] MATLAB 2018a, *The MathWorks Inc*, [SimScape Toolbox], Natick, MA, USA, 2018.

[36] A. M. Eltamaly, Y. Sayed Mohamed, A.-H. M. El-Sayed, A. Nasr, and A. Elghaffar, "Adaptive static synchronous compensation techniques with the transmission system for optimum voltage control," *Ain Shams Engineering Journal*, vol. 11, no. 1, pp. 35–44, 2020.

[37] E. Boulaoutaq, Y. Baala, S. Mouslime, M. Oubella, M. Kourchi, and A. Rachdy, "Enhanced LVRT capability of wind turbine based on DFIG using dynamic voltage restorer controlled by ADRC-based feedback control," *E3S Web of Conferences*, vol. 229, no. 1016, pp. 1–9, 2021.

[38] G. Ahmed, Y. Mohmed, and O. Kamel, "Optimal STATCOM Controller for Enhancing Wind Farm Power System Performance under Fault Conditions," in *Proceedings of the 2016 Eighteenth International Middle East Power Systems Conference (MEPCON)*, Cairo, Egypt, December 2016.

[39] M. A. Sahib and B. S. Ahmed, "A new multiobjective performance criterion used in PID tuning optimization algorithms," *Journal of Advanced Research*, vol. 7, no. 1, pp. 125–134, 2016.

[40] H. M. Hasanien and M. Matar, "Water cycle algorithm-based optimal control strategy for efficient operation of an autonomous microgrid," *IET Generation, Transmission & Distribution*, vol. 12, no. 21, pp. 5739–5746, 2018.

[41] M. Juybari, M. Ardakan, and H. Davari-Ardakani, "An adjusted water cycle algorithm for solving reliability-redundancy allocation problems with cold-standby components," *International Journal of Supply and Operations Management*, vol. 5, no. 3, pp. 218–233, 2018.

[42] E. M. Badr and H. Elgendy, "A hybrid water cycle-particle swarm optimization for solving the fuzzy underground water confined steady flow," *Indonesian Journal of Electrical Engineering and Computer Science*, vol. 19, no. 1, pp. 492–504, 2020.

[43] A. Sadollah, H. Eskandar, H. M. Lee, D. G. Yoo, and J. H. Kim, "Water cycle algorithm: a detailed standard code," *Software*, vol. 5, pp. 37–43, 2016.

[44] T.-Y. Wu, Y.-Z. Jiang, Y.-Z. Su, and W.-C. Yeh, "Using simplified swarm optimization on multiloop fuzzy PID controller tuning design for flow and temperature control system," *Applied Sciences*, vol. 10, pp. 1–23, 2020.

[45] T. Eswaran and V. S. Kumar, "Particle swarm optimization (PSO)-based tuning technique for PI controller for management of a distributed static synchronous compensator (DSTATCOM) for improved dynamic response and power quality," *Journal of Applied Research and Technology*, vol. 15, no. 2, pp. 173–189, 2017.

[46] M. A. Hossain, H. R. Pota, S. Squartini, and A. F. Abdou, "Modified PSO algorithm for real-time energy management in grid-connected microgrids," *Renewable Energy*, vol. 136, pp. 746–757, 2019.

[47] Y. Zhang, L. Zhang, and Z. Dong, "An MEA-tuning method for design of the PID controller," *Mathematical Problems in Engineering*, Hindawi, vol. 2019, pp. 1–11, Article ID 137878, 2019.

[48] H. Awad and A. Hafez, "Optimal operation of under-frequency load shedding relays by hybrid optimization of particle swarm and bacterial foraging algorithms," *Alexandria Engineering Journal*, vol. 61, no. 1, pp. 763–774, 2022.

[49] I. Elzemeity, M. Kotb, S. Kaddah, and M. El-Saadawi, "Improving voltage stability of doubly fed induction generator - based wind farm using STATCOM," *Mansoura Engineering Journal*, vol. 44, no. 2, pp. 19–25, 2019.

[50] S. Essallah, A. Bouallegue, and A. Khedher, "AVR and PSS controller integration in a power system: small-signal stability study with DFIG," *IEEE/CAA Journal of Automatica Sinica*, vol. 1, no. 1, pp. 55–65, 2018.

[51] L. Shi, S. Dai, L. Yao, Y. Ni, and M. Bazargan, "Impact of wind farms of DFIG type on power system transient stability," *Journal of Electromagnetic Analysis and Applications*, vol. 02, no. 08, pp. 475–481, 2010.

[52] S. El-Samanoudy, E.-S. Osman, M. El-Said, and M. El-Shaer, "Voltage stability of electrical power Networks with high penetration level of wind generation," *Journal of Al-Azhar University Engineering Sector*, vol. 15, no. 55, pp. 538–545, 2020.

[53] F. Arredondo, E. Castronuovo, P. Ledesma, and Z. Leonowicz, "Analysis of numerical methods to include dynamic constraints in an optimal power flow model," *Energies*, vol. 12, p. 885, 2019.

[54] A. Yakout, W. Sabry, and H. M. Hasanien, "Enhancing rotor angle stability of power systems using marine predator algorithm based cascaded PID control," *Ain Shams Engineering Journal*, vol. 12, no. 2, pp. 1849–1857, 2021.